Intraligand Excited States Turn a Ruthenium Oligothiophene Complex into a Light-Triggered Ubertoxin with Anticancer Effects in Extreme Hypoxia

John A. Roque III,^{a,b,§,#} Houston D. Cole,^{a,§} Patrick C. Barrett,^{b,§} Liubov M. Lifshits,^{a,#} Rachel O. Hodges,^{b,†} Susy Kim,^c Gagan Deep,^c Antonio Francés-Monerris,^d Marta E. Alberto,^{e*} Colin G. Cameron,^{a*} Sherri A. McFarland^{a*}

ABSTRACT

Ru(II) complexes that undergo photosubstitution reactions from triplet metal-centered (³MC) excited states are of interest in photochemotherapy (PCT) for their potential to produce cytotoxic effects in hypoxia. Dual-action systems that incorporate this stoichiometric mode to complement the oxygen-dependent photosensitization pathways that define photodynamic therapy (PDT) are poised to maintain antitumor activity regardless of oxygenation status. Herein, we examine the way in which these two pathways influence photocytotoxicity in normoxia and in hypoxia using the $[Ru(dmp)_2(IP-nT)]^{2+}$ series (where dmp=2,9-dimethyl-1,10-phenanthroline and IPnT=imidazo[4,5-f][1,10]phenanthroline tethered to n=0-4 thiophene rings) to switch the dominant excited state from the metal-based ³MC state in the case of Ru-phen-Ru-1T to ligand-based ³ILCT state for **Ru-3T** and **Ru-4T**. **Ru-phen–Ru-1T**, having dominant ³MC states and the largest photosubstitution quantum yields, were inactive in both normoxia and hypoxia. Ru-3T and Ru-4T, with dominant ³IL/³ILCT states and long triplet lifetimes (τ_{TA}=20–25 μs), had the poorest photosubstitution quantum yields yet were extremely active. In the best instances, Ru-4T exhibited attomolar phototoxicity toward SKMEL28 cells in normoxia and picomolar in hypoxia, with PI values in normoxia of 10⁵–10¹² and 10³–10⁶ in hypoxia. While maximizing excited state deactivation through photodissociative ³MC states did not result in bonafide dual-action PDT/PCT agents, the study has produced the most potent photosensitizer we know of to date. The extraordinary photosensitizing capacity of Ru-3T and Ru-4T may stem from a combination of very efficient ¹O₂ production and possibly complementary Type I pathways via ³ILCT excited states.

1. INTRODUCTION

Cancer remains a global health problem¹ despite recent advances in targeted and immunotherapies that complement standard treatments such as chemotherapy, radiotherapy, and surgery. Photodynamic therapy (PDT) is an alternate approach that has been used in

^aDepartment of Chemistry and Biochemistry, The University of Texas at Arlington, Arlington, Texas, 76019-0065 United States

^bDepartment of Chemistry and Biochemistry, The University of North Carolina at Greensboro, Greensboro, North Carolina 27402, USA

Department of Cancer Biology, Wake Forest School of Medicine, Winston Salem, NC, 27157 USA

^dDepartament de Química Física, Universitat de València, 46100 Burjassot, Spain

^eDipartimento di Chimica e Tecnologie Chimiche, Università della Calabria, Arcavacata di Rende, 87036 Italy §These authors contributed equally.

^{*}Corresponding Authors: M.E.A. <marta.alberto@unical.it> ORCID 0000-0001-9925-7233; C.G.C <colin.cameron@uta.edu> ORCID 0000-0003-0978-0894; S.A.M. <sherri.mcfarland@uta.edu> ORCID 0000-0002-8028-5055

combination with or in place of existing treatment modalities.^{2–9} PDT is a highly selective light-activated prodrug regimen that combines a photosensitizer (PS), light, and oxygen to induce toxicity that is spatially and temporally confined to cancerous tissue. Catalytic production of reactive oxygen species (ROS) (Scheme 1) generally leads to localized photocytotoxicity and tumor destruction. While PDT has historically been thought of as a local treatment, it has the capacity to induce an antitumor immune response that can eliminate distant metastases and afford long-term protection against recurrence.^{10–23} Over the past 20 years, the immunogenic response by PDT has been documented clinically^{24–29} and continues to be explored for its protective role.

Because the PDT response is impacted when oxygen supply is low, recent efforts have focused on developing light-responsive compounds that exploit oxygen-independent phototoxic pathways in order to maintain efficacy in hypoxia, which is a characteristic of some of the most aggressive and drug-resistant tumors. 30-34 Photochemotherapy (PCT), otherwise known as photoactivated chemotherapy (PACT), is the general term that has emerged to refer to these oxygen-independent photoprocesses. Ru(II) complexes serve as excellent prospects for PCT due in part to their ease of modification and tunability in terms of physical and chemical properties as well as their biological and photophysical profiles. Importantly, a variety of excited state configurations (e.g., metal-to-ligand charge transfer, MLCT; metal-centered, MC; intraligand, IL; intraligand charge transfer, ILCT; ligand-to-ligand charge transfer, LLCT; metal-to-metal-charge transfer, MMCT) can be accessed through rational design whereby ligand combinations are selected to alter or tune the excited state reactivity. 7,35-41 One notable PCT strategy exploits dissociative triplet MC excited state (3MC) for ligand photosubstitution in distorted Ru(II) complexes. The basic premise is that light promotes loss of a strain-inducing ligand, and the resulting Ru(II) photosubstitution product(s) and/or the liberated ligand⁴²⁻⁴⁴ ultimately lead to cell death (Scheme 1). This process is reminiscent of the mechanism of action of cisplatin, but triggered by light. Glazer and coworkers have previously shown that both 6.6'-dimethyl-2.2'bipyridine (dmb)^{45–49} and 2,9-dimethyl-1,10-phenanthroline (dmp)^{50–52} ligands undergo photosubstitution in bis-heteroleptic Ru(II) complexes by lowering the energy of the ³MC state through steric crowding in the metal coordination sphere. Likewise Turro^{53–64} and Bonnet^{65–68,43,69–} ⁷¹ have also exploited photolability for PCT in a variety of bis- and tris-heteroleptic Ru(II) scaffolds featuring combinations of tetra-, tri-, bi-, and monodentate ligands with emphasis on photocaged drug delivery.

Scheme 1. General reaction scheme for PDT versus PCT.

Several studies have demonstrated this oxygen-independent photochemistry in hypoxia under cell-free conditions, $^{68,72-75}$ and examples of phototoxic responses toward cancer cells growing in hypoxia are starting to emerge. Reliable strategies for maintaining hypoxia and assessing the dissolved oxygen concentration at the time of illumination have proven difficult but are now beginning to materialize, $^{68,73,75-77,79-86}$ making it possible to examine the potential of PCT agents as hypoxia-active phototherapeutics. In collaboration with the Glazer group, we published the most active PCT agent (at the time)— with [Ru(6,6'-dmb)₂(1-NIP)]Cl₂ and a phototherapeutic index of 15 (PI, ratio of dark to light EC₅₀ values) at 1% O₂ using visible light, where 1-NIP is 2-(naphthalen-1-yI)-1*H*-imidazo[4,5-*f*][1,10]phenanthroline. Bonnet and coworkers have since achieved a PI near 16 under 1% O₂.

The PIs demonstrated thus far for PCT agents are marginal but nonetheless notable since they are maintained under both normoxic (\sim 18.5–21% O_2)⁸⁷ and hypoxic (1% O_2) conditions. However, the stoichiometric nature of PCT is self-limiting relative to the catalytic PDT reactions. Thus, dual-action PDT/PCT agents that combine both modes (i.e., high ROS production alongside photolability) to elicit maximal activity in both normoxia and hypoxia are of interest. Such systems should generate the larger PI values that would be expected from catalytic photosensitization pathways in normoxia, and simultaneously have the capacity to utilize the less efficient PCT pathway in hypoxia.

Inspired by previous examples of dual-action PDT/PCT agents, 45,52,54,64,88 we have shown that complexes of the type $[Ru(6,6'-dmb)_2(IP-nT)]^{2+}$ (n=3, 4 thiophenes; IP=1H-imidazo[4,5f[[1,10]phenanthroline) undergo photoinduced ligand loss, leading to substitution of the straininducing 6,6'-dmb ligand for solvent molecules, while maintaining moderately-high ¹O₂ quantum yields (Φ_{Δ}) of 42-43% for the intact complex.^{78,88} Because the $[Ru(6,6'-dmb)_2(IP-4T)]^{2+}$ complex was substantially more photocytotoxic in normoxia relative to its IP-3T counterpart (PI=3400-3800 versus 400-600), it was investigated more rigorously (four cell lines, normoxia and 1% hypoxia) alongside its close relative [Ru(2,9-dmp)₂(IP-4T)]²⁺ (where 2,9-dmp=2,9-dimethyl-1,10phenanthroline, compound Ru-4T in Chart 1), also with strain-inducing polypyridyl ligands substituted with methyl groups. From this comparative study using four different cancer cell lines, several surprising findings emerged. 78 First, the identity of the coligand made a marked difference on the photoactivity of the complexes, with 2,9-dmp in the case of Ru-4T being superior to 6,6'dmb in [Ru(6,6'-dmb)₂(IP-4T)]Cl₂. Second, [Ru(6,6'-dmb)₂(IP-4T)]Cl₂ was completely inactive in 1% hypoxia in most of the cell lines despite undergoing photoinduced ligand loss in deoxygenated, cell-free solutions. Finally, and most important to the present study, Ru-4T gave nanomolar photocytotoxicities and unprecented PIs (as large as 5,900) with visible light in hypoxia (1% O₂). Together, these observations inspired the work described herein to determine whether Ru-4T acts as a true dual-action PDT/PCT agent or whether this metal complex is more likely an extremely efficient ROS generator given that 1% hypoxia in our condition still yields low concentrations of dissolved oxygen (6-9 µM).

The present study explores 2,9-dmp as the strain-inducing ligand in the **Ru-phen–Ru-4T** family (Chart 1). We hypothesized that varying the ILCT energies through thiophene chain extension would have minimal effect on the ³MLCT excited state energies but would serve to preferentially lower the ³ILCT state energies. Specifically, we aimed to switch the dominant excited state from the metal-based ³MC state in the case of **Ru-phen–Ru-1T** to the ligand-based ³ILCT state for **Ru-3T** and **Ru-4T** to determine the relationship between the photophysical and photochemical properties of these Ru(II) complexes and their photocytotoxicity profiles toward

cancer cells in normoxia and hypoxia. If **Ru-4T** acts as a bonafide dual-action PDT/PCT agent, then systematically reducing its ROS-generating capacity by raising the ³ILCT energy (on going from NN=**IP-4T** to **IP-0T or phen**) should lead to measurable photocytotoxiciy in hypoxia.

Chart 1: Structures of the type $[Ru(2,9-dmp)_2(NN)]^{2+}$ or **Ru-NN** examined in this study. Isolated compounds are mixtures of Δ/Λ enantiomers.

2. MATERIALS AND METHODS

All compounds were fully characterized by synthetic, computational, spectroscopic, and (photo)biological means. Some synthetic detail is provided below while supporting methods, spectra, and tables are available in the supplemental information (SI).

2.1 Instrumentation

Microwave reactions were performed in a CEM Discover microwave reactor. Flash chromatography relied on the Teledyne Isco CombiFlash EZ Prep system with Silicycle SiliaSep silica flash cartridges (FLH-R10030B-ISO25). Size-exclusion chromatography was performed on a manual column packed with Sephadex® LH-20. NMR spectra were collected using Agilent 700 MHz NMR at the Joint School of Nanoscience and Nanoengineering (JSNN) at Greensboro. The chemical shifts are reported in parts per million (ppm) and were referenced to the residual solvent peaks. ESI mass spectra were obtained using a Thermo Fisher LTQ Orbitrap XL coupled to a Water's Acquity Ultra Performance Liquid Chromatography (UPLC) stack using a BEH C18 column at UNCG's Triad Mass Spectrometry facility. HPLC analyses were carried out on an Agilent/Hewlett Packard 1100 series instrument (ChemStation Rev. A. 10.02 software) using a Hypersil GOLD C18 column (Thermo 25005-254630, guard 25003-014001) with an A–B gradient

(40 min run, 1 mL min⁻¹, 25°C; 98% \rightarrow 5% A; A=0.1% formic acid in H₂O, B=0.1% formic acid in MeCN). Reported retention times are accurate to within \pm 0.1 min.

2.2 Synthesis

To our knowledge, compounds **Ru-0T** through **Ru-3T** are new and previously unpublished; data regarding **Ru-4T** is published in a separate communication by us and is included here for completeness and comparison. Ru(2,9-dmp)₂Cl₂·2H₂O, imidazo[4,5-f][1,10]phenanthroline (IP) ligands, and the IP-4T precursor 4T-CHO were prepared according to adapted literature procedures. Se-90 Synthetic procedures and characterization are provided for ligands IP and IP-4T and compounds **Ru-phen** through **Ru-4T**. All final products are characterized via HNMR, H-H COSY NMR, HPLC, and ESI+MS Figures S1—24. Compound **Ru-4T** required additional C, HNGC, and HNGC, and HMBC NMR experiments for full assignment of the quaterthiophene group. CI- salts of final complex products were obtained via anion metathesis on HCI-treated Amberlite IRA-410 resin (Alfa-Aesar, A1773436) with methanol as eluent and isolated *in vacuo*. Final complexes are a mixture of Δ/Λ isomers.

1*H-imidazo*[4,5-*f*][1,10]phenanthroline (IP). 1,10-phenanthroline-5,6-dione (2.10 g, 10 mmol), formaldehyde (360 mg, 12 mmol), ammonium acetate (15.4 g, 200 mmol) and glacial acetic acid (32 mL) were added to a round bottom flask and heated at reflux for 7 hours. NH₄OH was added dropwise until the solution was neutralized (50 mL). The precipitate was filtered using a fine sintered frit and washed with cold deionized water (250 mL) and cold diethyl ether (100 mL). Solids were dried under reduced pressure (2.1 g, 95%). ¹H NMR (400 MHz, DMSO-d₆, ppm): δ 9.03 (dd, J = 4.2, 1.6 Hz, 2H; a), 8.82 (d, J = 7.8 Hz, 2H; c), 8.46 (s, 1H; d), 7.82 (dd, J = 8.1, 5.4 Hz, 2H; b).

2-([2,2':5',2":5'",2"'-quaterthiophen]-5-yl)-1H-imidazo[4,5-f][1,10]phenanthroline (IP-4T). 1,10-phenanthroline-5,6-dione (175 mg, 0.83 mmol), 4T-CHO (200 mg, 0.56 mmol), and ammonium acetate (1.38 g, 18 mmol) were added to a 250 mL round-bottom flask with glacial acetic acid (100 mL). The orange mixture was heated at 100 °C for 96 hours. Once cooled, the reddish-brown mixture was neutralized with NH₄OH. The precipitate was vacuum filtered using a Buchner funnel and washed with cold deionized water (50 mL) and cold ether (100 mL) to obtain the desired product as a brown solid (279 mg, 91%). ¹H NMR (500 MHz, DMSO- d_6 , ppm): δ 9.05 (dd, J = 4.2, 1.7 Hz, 2H), 8.85 (d, J = 7.9 Hz, 2H), 7.88–7.81 (m, 3H), 7.57 (d, J = 4.7 Hz, 1H), 7.52 (d, J = 3.8 Hz, 1H), 7.48 (d, J = 3.9 Hz, 1H), 7.41–7.36 (m, 3H), 7.32 (d, J = 3.7 Hz, 1H), 7.13 (dd, J = 5.1, 3.5 Hz, 1H).

[Ru(2,9-dmp)₂(phen)]Cl₂ (**Ru-phen**). Ru(2,9-dmp)₂Cl₂·2H₂O (63 mg, 0.1 mmol) and 1,10-phenanthroline (18 mg, 0.1 mmol) were added to a microwave vessel containing argon-purged ethylene glycol (2.5 mL) and subjected to microwave irradiation at 180 °C for 15 minutes. The resulting dark red mixture was transferred to a separatory funnel with deionized water (20 mL) and CH₂Cl₂ (30 mL). After gentle mixing, the CH₂Cl₂ was drained and the remaining aqueous layer was washed with CH₂Cl₂ (30 mL portions) until the CH₂Cl₂ was colorless. At that point, another 30 mL of CH₂Cl₂ was added and allowed to settle to the bottom of the separatory funnel. Then, saturated aqueous KPF₆ (5 mL) was added, and the mixture was shaken gently and allowed to settle over time to facilitate transfer of the product from the aqueous layer to the CH₂Cl₂ layer, which was concentrated under reduced pressure. The crude product was purified by silica gel flash column chromatography with a gradient of MeCN, 10% water in MeCN, followed by 7.5% water in MeCN with 0.5% KNO₃ to obtain the desired product as an orange solid (93 mg, 94%).

The PF₆⁻ salt was converted in quantitative yield to its corresponding Cl⁻ salt using Amberlite IRA-410 with MeOH as the eluent. The solids were purified further using Sephadex LH-20 with MeOH as the eluent (36 mg, 50%). R_f = 0.23 (0.5% KNO₃, 7.5% H₂O, 92% MeCN). ¹H NMR (500 MHz, MeOD- d_3 , ppm): δ 8.82 (d, J = 8.4 Hz, 2H; 7,7'). 8.51 (dd, J = 8.2, 1.3 Hz, 2H; c,f), 8.38–8.33 (m, 4H; 6,6',4,4'), 8.19 (d, J = 8.8 Hz, 2H; 5,5'), 8.13 (s, 2H; d,e), 7.92 (d, J = 8.4 Hz, 2H; 8,8'), 7.51 (dd, J = 5.4, 1.2 Hz, 2H; a,h), 7.43 (dd, J = 8.2, 5.5 Hz, 2H; b,g), 7.33 (d, J = 8.3 Hz, 2H; 3,3'), 2.06 (s, 6H; 9,9'-Me), 1.75 (s, 6H; 2,2'-Me); (for hydrogen labels, see Figure S1). HRMS (ESI+) m/z: [M-2Cl]²⁺ Calcd for C₄₀H₃₂Cl₂N₆Ru: 349.0860; Found: 349.0856. [M-2Cl-H]⁺ Calcd for C₄₀H₃₁Cl₂N₆Ru: 697.1648; Found: 697.1636. HPLC retention time: 9.37 min (99% purity by peak area).

[$Ru(2,9-dmp)_2(IP)$] Cl_2 (**Ru-0T**). Ru(2,9-dmp)₂Cl₂·2H₂O (63 mg, 0.1 mmol) and IP (22 mg, 0.1 mmol) were combined and treated according to the procedure described for **Ru-phen** to yield a red solid (62 mg, 60%). The PF6⁻ salt was converted in quantitative yield to its corresponding Cl⁻ salt using Amberlite IRA-410 with MeOH as the eluent. The solids were purified further using Sephadex LH-20 with MeOH as the eluent (45 mg, 92%). R_f = 0.9 (0.5% KNO₃, 7.5% H₂O, 92% MeCN). ¹H NMR (500 MHz, MeOD- d_3 , ppm): δ 8.84–8.83 (m, 4H; 7,7′,c), 8.67 (s, 1H; d), 8.36 (t, 4H; 6,6′,4,4′), 8.19 (d, J = 8.8 Hz, 2H; 5,5′), 7.93 (d, J = 8.4 Hz, 2H; 8,8′), 7.50–7.46 (m, 4H; b,a), 7.33 (d, J = 8.4 Hz, 2H; 3,3′), 2.06 (s, 6H; 9,9′-Me), 1.79 (s, 6H; 2,2′-Me); (for hydrogen labels, see Figure S2). HRMS (ESI+) m/z: [M-2CI]²⁺ Calcd for C₄₁H₃₂Cl₂N₈Ru: 369.0891; Found: 369.0886. [M-2CI-H]⁺ Calcd for C₄₁H₃₁Cl₂N₈Ru: 737.1710; Found: 737.1699. HPLC retention time: 9.53 min (99% purity by peak area).

[$Ru(2,9\text{-}dmp)_2(IP\text{-}1T)$] Cl_2 (**Ru-1T**). Ru(2,9-dmp)₂Cl₂·2H₂O (100 mg, 0.16 mmol) and IP-1T (48 mg, 0.16 mmol) were combined and treated according to the procedure described for Ru-phen to yield a red solid (102 mg, 57%). The PF₆⁻ salt was converted in quantitative yield to its corresponding Cl⁻ salt using Amberlite IRA-410 with MeOH as the eluent. A portion of the Cl⁻ salt (46 mg) was purified further using Sephadex LH-20 with MeOH as the eluent (43 mg, 93%). R_f = 0.28 (0.5% KNO₃, 7.5% H₂O, 92% MeCN). ¹H NMR (500 MHz, MeOD- d_3 , ppm): δ 8.90 (d, J = 7.3 Hz, 2H; c), 8.28 (d, J = 8.4, 2H; 7,7′), 8.35 (dd, J = 8.7, 7.6 Hz, 4H; 6,6′,4,4′), 8.19 (d, J = 8.8 Hz, 2H; 5,5′), 7.94 (d, J = 1.0 Hz, 1H; f), 7.92 (d, J = 8.4 Hz, 2H; 8,8′), 7.69 (d, J = 4.4 Hz, 1H; d), 7.46–7.40 (m, 4H; b,a), 7.33 (d, J = 8.4 Hz, 2H; 3,3′), 7.26 (dd, J = 4.9, 4.0 Hz, 1H; e), 2.06 (s, 6H; 9,9′-Me), 1.81 (s, 6H, 2,2′-Me); (for hydrogen labels, see Figure S3). HRMS (ESI+) m/z: [M-2CI]²⁺ Calcd for C₄₅H₃₄Cl₂N₈RuS: 410.0830; Found: 410.0822. [M-2CI-H]⁺ Calcd for C₄₅H₃₃Cl₂N₈RuS: 819.1587; Found: 819.1580. HPLC retention time: 9.63 min (97% purity by peak area).

[Ru(2,9-dmp)₂(IP-2T)]Cl₂ (**Ru-2T**). Ru(2,9-dmp)₂Cl₂·2H₂O (63 mg, 0.1 mmol) and IP-2T (39 mg, 0.1 mmol) were combined and treated according to the procedure described for Ru-phen to yield a red solid (40 mg, 34%). The PF₆⁻ salt was converted in quantitative yield to its corresponding Cl⁻ salt using Amberlite IRA-410 with MeOH as the eluent. The Cl⁻ salt was purified further using Sephadex LH-20 with MeOH as the eluent (29 mg, 89%). R_f = 0.25 (0.5% KNO₃, 7.5% H₂O, 92% MeCN). ¹H NMR (500 MHz, MeOD- d_3 , ppm): δ 8.89 (d, J = 7.0 Hz, 2H; c), 8.82 (d, J = 8.4 Hz, 2H; 7,7′), 8.36 (dd, J = 8.8, 6.4 Hz, 4H; 6,6′,4,4′), 8.19 (d, J = 8.8 Hz, 2H; 5,5′), 7.93 (d, J = 8.4 Hz, 2H; 8,8′), 7.86 (d, J = 4.0 Hz, 1H; d), 7.48–7.42 (m, 5H; a,b,h), 7.39 (d, J = 3.1 Hz, 1H; f), 7.36 (d, J = 4.0 Hz, 1H; e), 7.34 (d, J = 8.4 Hz, 2H; 3,3′), 7.11 (dd, J = 5.1, 3.6 Hz, 1H, g), 2.06 (s, 6H; 9,9′-Me), 1.82 (s, 6H; 2,2′-Me); (for hydrogen labels, see Figure S4). HRMS (ESI+) m/z: [M-2Cl]²⁺ Calcd for C₄₉H₃₆Cl₂N₈RuS₂ 451.0768; Found: 451.0754. [M-2Cl-H]⁺ Calcd for

 $C_{49}H_{35}Cl_2N_8RuS_2$: 901.1464; Found: 901.1451. HPLC retention time: 21.67 min (98% purity by peak area).

[$Ru(2,9-dmp)_2(IP-3T)$] Cl_2 (**Ru-3T**). Ru(2,9-dmp)₂Cl₂·2H₂O (100 mg, 0.16 mmol) and IP-3T (75 mg, 0.16 mmol) were combined and treated according to the procedure described for Ru-phen to yield a red solid (116 mg, 57%). The PF₆⁻ salt was converted in quantitative yield to its corresponding Cl⁻ salt using Amberlite IRA-410 with MeOH as the eluent. The Cl⁻ salt was purified further using Sephadex LH-20 with MeOH as the eluent (85 mg, 89%). R_f = 0.38 (0.5% KNO₃, 7.5% H₂O, 92% MeCN). ¹H NMR (500 MHz, MeOD- d_3 , ppm): δ 8.89 (br s, 2H; c), 8.83 (d, J = 8.4 Hz, 2H; 7,7′), 8.36 (dd, J = 8.8, 5.6 Hz, 4H; 6,6′,4,4′), 8.20 (d, J = 8.8 Hz, 2H; 5,5′), 7.93 (d, J = 8.4 Hz, 2H; 8,8′), 7.87 (d, J = 4.0 Hz, 1H; d), 7.48–7.43 (m, 4H; a,b), 7.39–7.37 (m, 2H; j,e), 7.34 (d, J = 8.4 Hz, 2H; 3,3′), 7.32 (d, J = 3.9 Hz, 1; f), 7.29 (dd, J = 3.6, 1.1 Hz, 1H; h), 7.21 (d, J = 3.8 Hz, 1H; g), 7.07 (dd, J = 5.1, 3.7 Hz, 1H; i), 2.06 (s, 6H; 9,9′-Me), 1.82 (s, 6H; 2,2′-Me) (for hydrogen labels, see Figure S5). HRMS (ESI+) m/z: [M-2CI]²⁺ Calcd for C₅₃H₃₈Cl₂N₈RuS₃: 492.0707; Found: 492.0691. [M-2CI-H]⁺ Calcd for C₅₃H₃₇Cl₂N₈RuS₃: 983.1341; Found: 983.1330. HPLC retention time: 23.10 min (96% purity by peak area).

[Ru(2,9-dmp)₂(IP-4T)]Cl₂ (Ru-4T). Ru(2,9-dmp)₂Cl₂·2H₂O (100 mg, 0.16 mmol) and IP-4T (88 mg, 0.16 mmol) were combined and added to a microwave vessel containing argon-purged ethylene glycol (2.5 mL) and subjected to microwave irradiation at 180 °C for 15 minutes. The resulting dark red mixture was transferred to a separatory funnel with deionized water (20 mL) and CH₂Cl₂ (30 mL). After gentle mixing, the CH₂Cl₂ was drained and the remaining aqueous layer was washed with CH2Cl2 (30 mL portions) until the CH2Cl2 was colorless. At that point, another 30 mL of CH₂Cl₂ was added and allowed to settle to the bottom of the separatory funnel. Then, saturated aqueous KPF₆ (5 mL) was added, and the mixture was shaken gently and allowed to settle over time to facilitate transfer of the product from the aqueous layer to the CH₂Cl₂ layer, which was concentrated under reduced pressure. The crude product was purified by silica gel flash column chromatography with a gradient of MeCN, 10% water in MeCN, followed by 7.5% water in MeCN with 0.5% KNO₃ to obtain the desired product as a red solid (86 mg, 50%). The PF₆⁻ salt was converted in quantitative yield to its corresponding Cl⁻ salt using Amberlite IRA-410 with MeOH as the eluent. The Cl⁻ salt was purified further using Sephadex LH-20 (66 mg, 92%). $R_f = 0.32 (0.5\% \text{ KNO}_3, 7.5\% \text{ H}_2\text{O}, 92\% \text{ MeCN})$. ¹H NMR (700 MHz, MeOD- d_3 , ppm): δ 8.93 (bs, 2H; c), 8.82 (d, J = 8.4 Hz, 2H; 7,7'), 8.36 (d, J = 9.1 Hz, 2H; 6,6'), 8.35 (d, J = 8.4 Hz, 2H; 4,4'), 8.19 (d, J = 9.1 Hz, 2H; 5,5'), 7.92 (d, J = 8.4 Hz, 2H; 8,8'), 7.87 (d, J = 3.5 Hz, 1H; d), 7.46 (m, 2H; b), 7.44 (d, J = 5.6 Hz, 2H; a), 7.38 (d, J = 4.2 Hz, 1H; e), 7.35 (d, J = 4.9 Hz, 1H; l), 7.34 (d, J = 7.7 Hz, 2H; 3,3'), 7.33 (d, J = 3.5 Hz, 1H; f), 7.26 (d, J = 3.5 Hz, 1H; j), 7.23 (d, J = 4.2 Hz, 1H; g), 7.21 (d, J = 3.5 Hz, 1H; h), 7.16 (d, J = 3.5 Hz, 1H; i), 7.05 (dd, J = 4.9, 3.5 Hz, 1H; k), 2.06 (s, 6H; 9-Me), 1.82 (s, 6H; 2-Me) (for hydrogen labels, see Figure S6). ¹³C NMR (175 MHz, MeOH d_3 , ppm): δ 169.96 (9,9'), 168.19 (2,2'), 152.27 (a), 150.84 (20), 150.16 (10), 149.73 (21), 147.68 (22,24), 141.64 (12), 139.46 (7,7'), 138.49 (14), 138.26 (16), 138.20 (4,4'), 137.84 (17), 136.39 (15), 136.16 (13), 131.96 (c,23), 131.66 (11), 131.63 (18), 131.44 (19), 129.72 (d), 129.11 (k), 128.80 (6,6'), 128.59 (8), 128.53 (5,5'), 127.72 (3,3'), 126.96 (f), 126.26 (b), 126.09 (h,l), 125.87 (e), 125.81 (g), 125.57 (i), 125.12 (j), 26.97 (2,2'-Me), 25.46 (9,9'-Me) (for carbon labels, see Figure S7). HRMS (ESI+) m/z: [M-2CI]²⁺ Calcd for C₅₇H₄₀N₈RuS₄ 533.0646; Found: 533.0634. [M-2CI-H]⁺ Calcd for C₅₇H₃₉N₈RuS₄ 1065.1219; Found: 1065.1220. HPLC retention time: 24.35 min (98% purity by peak area).

3. RESULTS AND DISCUSSION

3.1 Synthesis and Characterization

Complexes **Ru-phen** and **Ru-nT** were synthesized following procedure similar to the one that we previously described for the synthesis of related Os(II) complexes.^{79,80} The complexes were isolated as their PF₆⁻ salts and purified with flash chromatography on silica, affording final products in 50% yields. The PF₆⁻ salts were converted to their corresponding Cl⁻ salts in quantitative yields via anion metathesis using Amberlite IRA-410 and were further purified using size-exclusion chromatography on Sephadex LH-20. HPLC analysis confirmed the purities of complexes to be 95% or higher (Figures S19–S24). The structures of complexes **Ru-phen–Ru-4T** were confirmed using high resolution ESI+ mass spectrometry (Figures S13–S18) and a detailed analysis of both their 1D ¹H NMR (Figure S1–S7) and 2D NMR spectra (Figures S1–S12). The ¹H NMR assignments of **Ru-phen** and **Ru-0T–Ru-3T** were made using ¹H–¹H COSY NMR in the same manner as other related compounds.⁷⁹ **Ru-4T** required additional 2D NMR experiments (¹H–¹³C HSQC NMR, ¹H–¹³C HMBC NMR) for full assignment of the quaterthiophene unit. The resulting assignments for all of the complexes are shown in Figure 1.

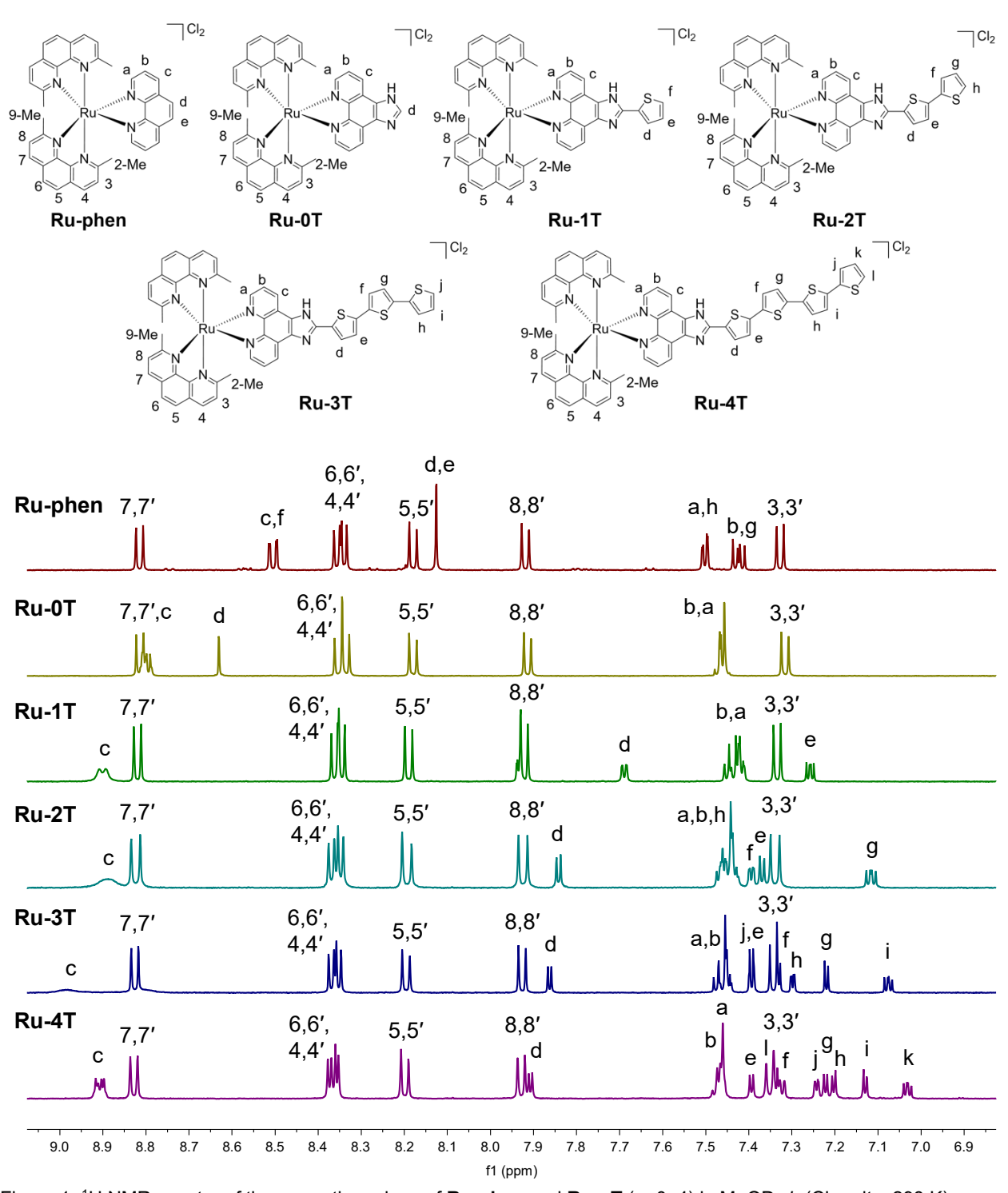


Figure 1. 1 H NMR spectra of the aromatic regions of **Ru-phen** and **Ru-nT** (n=0–4) in MeOD- d_3 (Cl $^-$ salts; 298 K) collected at 500 MHz except for **Ru-4T**, which was collected at 700 MHz.

3.2 Computational Studies

Additional computational details can be found in Tables S1–S6 and Figures S25–S35 in the Supplementary Information.

3.2.1 Ground state configuration

Ground state singlet and excited triplet state properties of **Ru-phen** and **Ru-nT** (n=1-4) were explored by using DFT and TD-DFT calculations. Geometry optimizations were obtained in water, and the structures for the singlet ground state are depicted in Figure 2. The ground states consist of the central metal ion in pseudo-octahedral geometry with the rings of the oligothiophenes along the series adopting an almost coplanar trans conformation (Figure 2, Table S5). The planarity of the rigid IP ligand extends to the first electron-donating thiophene ring, with additional rings (n=2-4) leading to increased conformational flexibility whereby the fourth ring is twisted up to 19° relative to the IP plane.

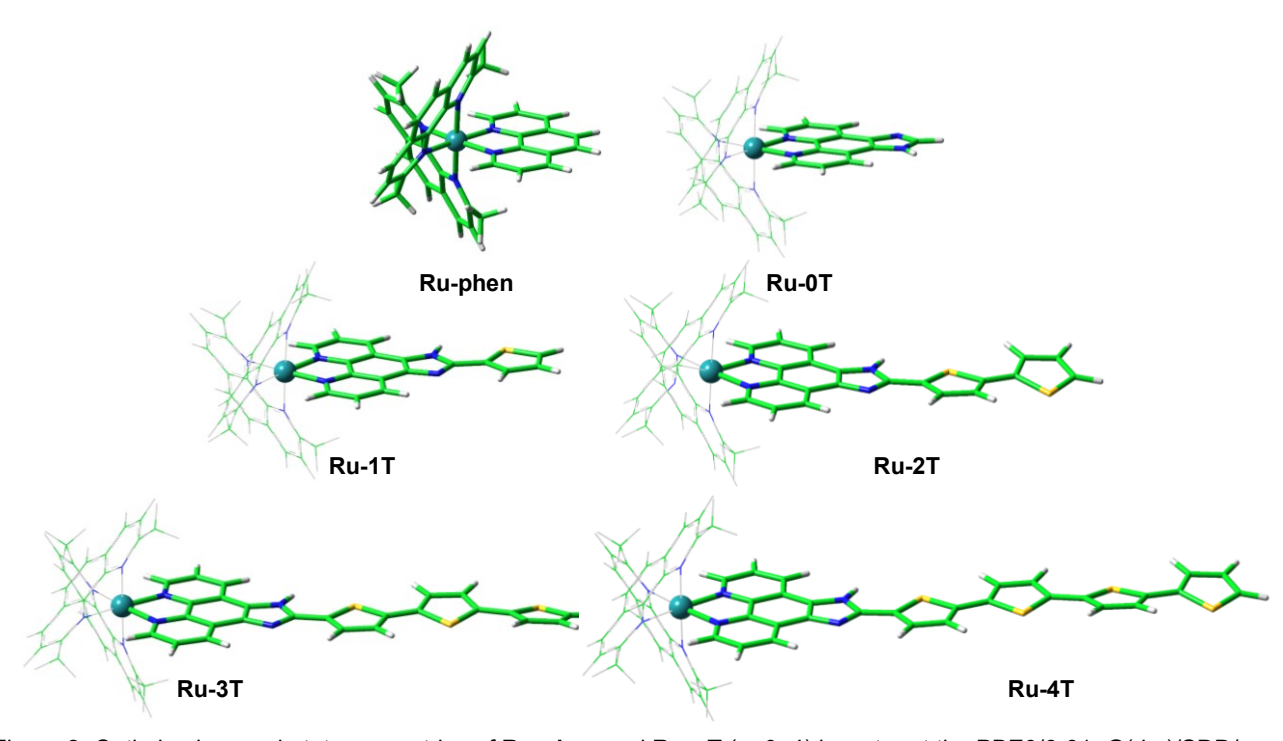


Figure 2. Optimized ground-state geometries of **Ru-phen** and **Ru-nT** (n=0–4) in water at the PBE0/6-31+G(d,p)/SDD/ level of theory.

The ground state electronic structures of the complexes were characterized according to their frontier molecular orbitals (HOMO-1, HOMO, LUMO, LUMO+1; Figure S26). Similar to what we have previously observed for our related Ru(II) and Os(II) complexes bearing IP-nT ligands, ^{79,80,91} the nature of the HOMO orbital changes with increasing n, concomitant with an increase in its energy and subsequent reduction of the HOMO-LUMO gap (Figure 3 and Table S1), with relatively little impact on the LUMO energy.

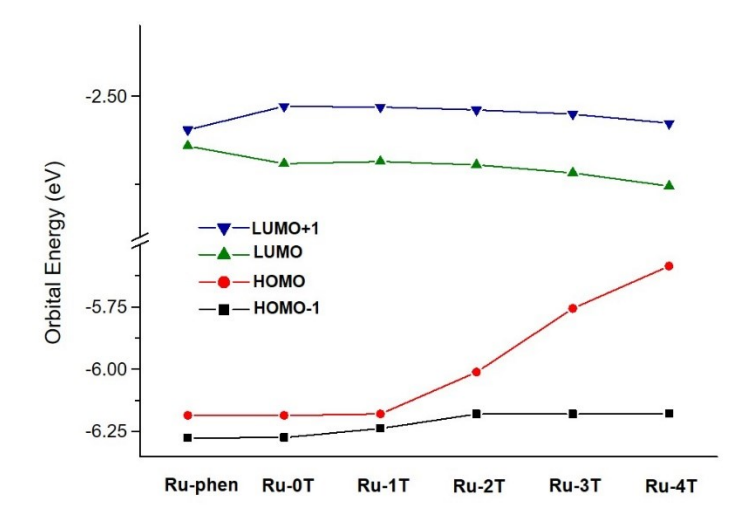


Figure 3. Calculated frontier orbital energies and H-L gaps (eV) for the compounds of this study.

The HOMO orbitals of **Ru-phen**, **Ru-0T**, and **Ru-1T** are predominantly metal-based (≈37%; Table 1 and Figure 4). This metal character disappears for **Ru-2T**, **Ru-3T**, **and Ru-4T**, where the contribution of the oligothiophene chain becomes progressively greater (29, 53, and 67%, respectively) with minimal metal character. The destabilization of HOMO energy (Table S1) is directly related to the (oligo)thienyl contribution to the orbital. In sharp contrast, the lack of any (oligo)thienyl contribution to the metal-based HOMO−1 orbital is the reason why the energies of these orbitals do not appreciably change along the series. The significant Ru(*d*π) contribution to these orbitals is associated with substantial phen ligand mixing for **Ru-phen** and for **Ru-2T** through **Ru-4T**, and this mixing extends to the IP ligand for **Ru-0T** and **Ru-1T** (Table 1, Figures S26 and S28).

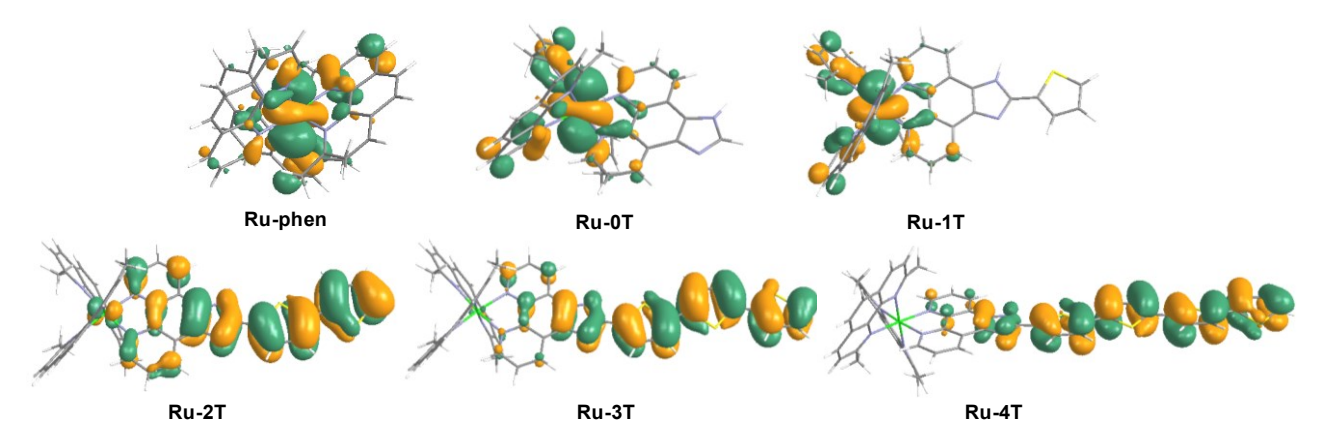


Figure 4. Ru(II)-based HOMOs for Ru-phen, Ru-0T, and Ru-1T and (oligo)thienyl-based HOMOs for Ru-nT (n=2–4), computed at the M0-6/6-31+G(d,p)/SDD level of theory in water.

Table 1. Calculated percent contribution of the Ru(*d*π) Orbitals and the phen, IP, and (oligo)thienyl Orbitals to the Frontier Orbitals (HOMO-1, HOMO, LUMO, LUMO+1) for **Ru-phen** and **Ru-nT** (*n*=0–4) in the Singlet Ground State (¹GS)

	HOMO-1			НОМО			LUMO			LUMO+1						
%	Ru	Phen	ΙP	nТ	Ru	Phen	ΙP	пT	Ru	Phen	ΙP	nТ	Ru	Phen	ΙP	nТ
Ru-phen	27	73	/	/	37	63	/	1	3	97	/	/	7	93	/	/
Ru-0T	26	45	29	/	38	56	7	/	3	78	19	/	6	75	19	1
Ru-1T	20	20	48	2	37	56	7	0	3	78	19	0	6	77	17	0
Ru-2T	37	56	6	0	1	32	38	29	3	75	20	2	6	76	17	1
Ru-3T	37	56	6	0	0	27	19	53	3	72	21	4	6	75	17	2
Ru-4T	37	56	7	0	0	21	12	67	4	62	23	12	5	74	17	4

The LUMO and LUMO+1 orbitals are primarily ligand-based, with the most predominant contribution coming from the phen portion of the IP ligands. The slight stabilization of these LUMOs on going from **Ru-1T** to **Ru-4T** is consistent with an increased contribution from the (oligo)thienyl group that exerts an effect opposite to the energy trend of the HOMO orbitals, as already observed in similar complexes. The corresponding reduction of HOMO-LUMO gaps along the series correlates with the red-shift of the (oligo)thienyl-associated absorption bands (and their increased intensity throughout the visible region) as n increases. Inspection of the computed spectra (Figure S27) and the orbital contribution to each transition (Figure S29, Table S3) was used to assign the lowest-energy spin-allowed, singlet—singlet bands in the experimental absorption spectra. The nature of these transitions changes with n, from predominant nLCT character for n1 to mixed n1 LCT/n1 character in the case of n1 and n2 to mixed n3 the HOMOs mainly extend over the oligothiophene chain. Natural transition orbital (NTO) plots (Figures S29) support the nature of the computed states. Additional details on the spectra, orbital composition, and assignment of the lowest 10 vertical singlet—singlet transitions can be found in Figures S25—S29 and Tables S2–S4.

3.2.2 Excited state calculations and feasibility of Type II photoreactions

The lowest-energy triplet excited states (T_1) adopt a fully planar arrangement of the (oligo)thiophene chain having maximal π -conjugation, in agreement with what has been reported for free oligothiophenes^{92,93} and with what was previously found for related Ru(II) and Os(II) analogs.^{79,80,91} As expected, the Ru-N bond lengths do not vary for the T_1 optimized geometries. A comparison of the optimized singlet and triplet geometries is reported in Figure S30 and Table S5, respectively.

The nature and the energy of the triplet state is strongly influenced by the length of the oligothienyl chain. The vertical singlet–triplet splitting (Δ_{S0-T1}), representing the T_1 energy, computed in water for each compound is shown in Figure S31 and summarized in Table 2. The lowest-lying triplet states are sufficient in energy to produce singlet oxygen (computed to be 0.90 eV⁹⁴ versus 0.97 eV⁹⁵ by experiment). While **Ru-phen**, **Ru-0T** and **Ru-1T** have similar S_0-T_1 gaps, additional thiophenes cause a systematic decrease in these energy gaps, reaching values as low as 1.71 eV for **Ru-4T**.

The abrupt drop in energy for the lowest-lying triplet state of \mathbf{Ru} - \mathbf{n} with $\mathbf{n} \ge 2$ is directly related to a change from primarily ${}^3\mathrm{MLCT}$ to ${}^3\mathrm{ILCT}/{}^3\mathrm{IL}$ character, consistent with thienyl chain extension. Mulliken spin densities close to one on the Ru(II) center for $\mathbf{n} < 2$ (≈ 0.80) is indicative of one unpaired electron on the metal center in the excited state as would be expected for the ${}^3\mathrm{MLCT}$ state, which is further corroborated by the NTOs reported in Figure S32. In contrast, metal involvement was not detected for complexes bearing two, three and four thienyl groups, in agreement with the assignment of the lowest-energy triplet states in these complexes as ${}^3\mathrm{ILCT}/{}^3\mathrm{IL}$ states. Predominant intraligand transitions were previously connected to longer lifetimes in both Ru(II) and Os(II) complexes. ${}^{7,88,90,79,80,96-99}$

Table 2. Calculated T_1 energy and lowest 3MC energy for **Ru-phen** and **Ru-nT** (n=0–4). MSD = Mulliken Spin Density on the Ru metal center (no metal involvement was found for n≥2). Vertical lowest 3MC states provided in parentheses.

	T ₁ energy (eV)	Configuration	MSD	Lowest ³ MC energy (eV)
Ru-phen	2.35	³ MLCT	0.77	2.53 (T ₆)
Ru-0T	2.32	³ MLCT	0.75	2.54 (T ₆)
Ru-1T	2.32	³ MLCT	0.74	2.53 (T ₆)
Ru-2T	2.16	³ ILCT/ ³ IL	0	2.52 (T ₇)
Ru-3T	1.87	3ILCT/3IL	0	2.73 (T ₁₃)
Ru-4T	1.71	3ILCT/3IL	0	2.70 (T ₁₃)

Inspection of the lowest-lying triplet excited states (T_1-T_{14}) in the Frank-Condon region (Table S6) reveals the presence of states with predominant 3MC character at relatively low energies for **Ru-phen** and for **Ru-nT** with $n \le 2$ (≈ 2.50 eV). However, with more than two thienyl groups (**Ru-3T** and **Ru-4T**), the 3MC state is higher in energy (~ 2.70 eV). The nature of these higher-lying 3MC states is supported by their calculated NTO topologies (Figure S33).

3.3 Spectroscopy

3.3.1 UV-Visible absorption and emission

absorption normalized electronic spectra for Ru-phen-Ru-4T their hexafluorophosphate (left) and chloride (right) salts in MeCN and water, respectively, are shown in Figure 5. The corresponding molar extinction coefficients for the local peak maxima in these spectra are listed in Table 3. Regardless of the counter ion and solvent, there are three major transitions that characterize the spectra. The more intense $\pi \rightarrow \pi^*$ transitions involving the 2,9dmp ligands and the proximal portion of the IP/IP-nT ligands occur below 300 nm and are similar for all of the complexes. The less intense peaks that appear just past 450 nm (somewhat obscured in **Ru-3T** and **Ru-4T**) correspond to the Ru²⁺(d π) \rightarrow LL(π *) MLCT transitions that involve both the metal center and the ligands (LL). These transitions are largely unaffected by the thienyl groups, indicating similar acceptor orbitals among the complexes contributed by the 2,9-dmp ligands and/or the phen portion of the IP-based ligands. The most distinguishing features of the spectra are the (oligo)thienvl-based $\pi \rightarrow \pi^*$ transitions that occur near 340 nm for **Ru-1T** and move toward progressively longer wavelengths with extension of the thiophene chain. These lower-energy $\pi \rightarrow \pi^*$ transitions do not appear to exhibit a significant solvent or counter ion dependence for complexes Ru-1T- Ru-3T. The exception is Ru-4T, where both the relative intensities and

energies of the oligothiophene-based transitions change with counter ion and solvent (Figure S36). We ascribe the solvatochromic behavior of **Ru-4T** to a larger degree of CT character with respect to the ILCT state.

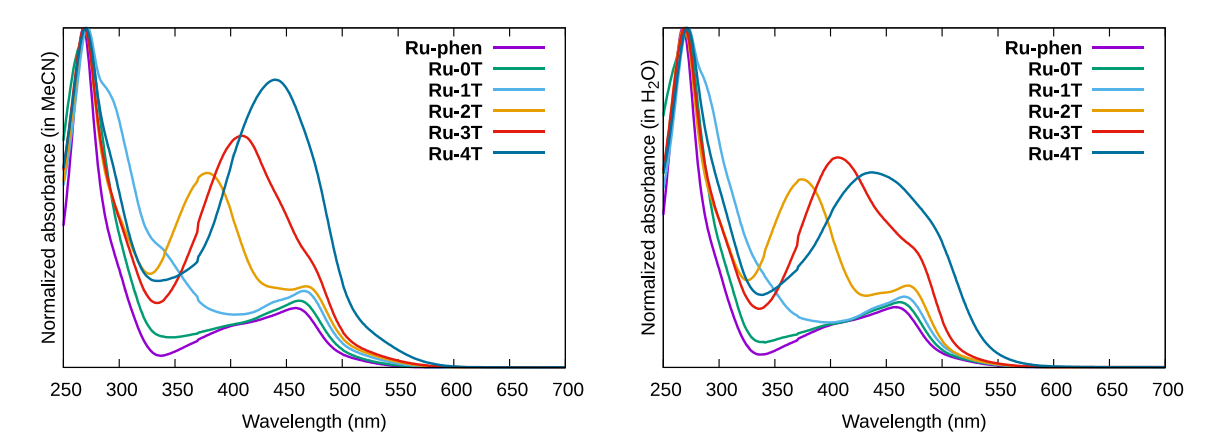


Figure 5: UV-Vis absorption spectra of **Ru-phen–Ru-4T** as PF₆⁻ salts in MeCN (left) and as Cl⁻ salts in water (right). The spectra are normalized to the peak near 270 nm. Alternative overlays are shown in Figure S36.

Table 3. UV-Vis absorption peak	maxima and m	olar extinction coefficie	ents for Ru-phen – Ru-4T .

Cmpd	λ_{max} /nm (log ϵ) in MeCN	λ _{max} /nm (log ε) in water
Ru-phen	209 (4.99), 268 (4.98), 458 (4.22)	268 (4.84), 298 (4.33), 395 (3.92), 460 (4.09)
Ru-0T	213 (4.91), 271 (4.89), 462 (4.18)	271 (4.81), 305 (4.31), 400 (3.93), 464 (4.10)
Ru-1T	214 (4.95), 272 (4.91), 466 (4.27)	273 (4.82), 288 (4.75), 340 (4.26), 442 (4.06), 466 (4.13)
Ru-2T	212 (4.92), 269 (4.89), 379 (4.65), 467 (4.27)	269 (4.82), 299 (4.47), 376 (4.56), 447 (4.16), 470 (4.20)
Ru-3T	211 (4.95), 269 (4.93), 410 (4.76)	270 (4.85), 299 (4.50), 406 (4.64), 477 (4.38)
Ru-4T	206 (4.94), 270 (4.88), 440 (4.80)	272 (4.90), 436 (4.66), 488 (4.54)

The steady state emission associated with the complexes was measured for dilute (\approx 5 µM) solutions in argon-sparged acetonitrile. The strong 3 MLCT phosphorescence that is well-known for Ru(II) polypyridyl complexes, 35 e.g., 9.5% for [Ru(bpy)₃]²⁺, 100 was completely absent even in deaerated solution. Therefore, it was concluded that the triplet excited states for these compounds decay primarily through nonradiative pathways.

3.3.2 Transient absorption

Given that the primary triplet state(s) involved in the excited state relaxation of the complexes were nonemissive, these states were interrogated by nanosecond transient absorption (TA) at room temperature in degassed MeCN solution. **Ru-phen**, **Ru-0T**, and **Ru-1T** did not produce any transients in the nanosecond to microsecond regime. The absence of ³MLCT or ³IL signatures in the excited state absorption (ESA) spectra suggests that these states do not contribute to excited state relaxation for these compounds on this timescale, which is consistent with the fact that the ³MLCT state was undetectable in the steady-state emission experiments. This finding is in line with what would be expected for excited state deactivation through the ³MC pathway.

Compounds **Ru-2T**–**Ru-4T**, however, gave strong TA signals. The ESA spectra collected at 10 nm intervals are shown in Figure 6. The full time-sliced ESA spectra are in Figure S38 and the TA lifetimes are compiled in Table 4.

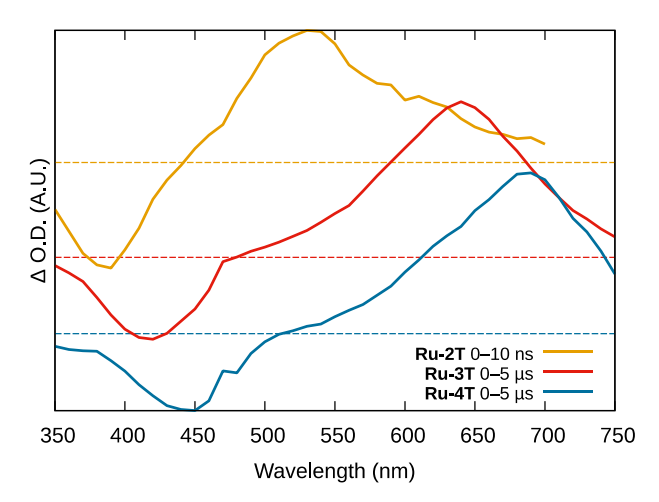


Figure 6: Transient absorption spectra of **Ru-2T–Ru-4T** integrated over the indicated time slice following the excitation pulse. The color-keyed dashed line indicates $\Delta_{O.D.}$ =0.

Each ESA spectrum for **Ru-2T**–**Ru-4T** is a superposition of the bleach from the strong IL/ILCT and MLCT ground-state absorptions (Figure 5) with a broad new positive feature at longer wavelengths that is attributed to transitions associated with the lowest-lying ³IL/³ILCT state. The signatures of the **Ru-3T** and **Ru-4T** transients match those of the free IP-3T and IP-4T ligands, which are published elsewhere, ^{79,80} with ESA maxima that shift to longer wavelengths with increasing *n*. The ESA maxima for **Ru-2T**–**Ru-4T** occur near 525–550, 625–650, and 675–700 nm, respectively, and reflect increased conjugation of the planar T₁ state as the oligothiophene chain is lengthened. The TA lifetimes were monoexponential, shorter for **Ru-2T** (around 5.8–7.9×10² ns), and substantially longer for **Ru-3T** and **Ru-4T** (around 23–25 μs and 20–24 μs, respectively). These time constants were wavelength-independent and assigned unambiguously to the ³IL/³ILCT state for **Ru-3T** and **Ru-4T**. The much shorter T₁ lifetime for **Ru-2T** despite its higher-lying ³IL/³ILCT (relative to **Ru-3T** and **Ru-4T**) suggests that an excited state equilibrium may exist with the ³MLCT state due to its energetic proximity.

3.3.3 Singlet oxygen

Singlet oxygen quantum yields were calculated in accordance with Equation S1 from the intensity of the ${}^{1}O_{2}$ phosphorescence, measured at room temperature in air-saturated MeCN with $[Ru(bpy)_{3}](PF_{6})_{2}$ as the standard $(\Phi_{\Delta,S}=0.56^{101})$. The results are tabulated in Table 4. The calculated ${}^{1}O_{2}$ quantum yields assume negligible photodissociation and/or photobleaching during the emission scan, which is based on recording non-averaged, single emission scans collected with a fast scan rate.

The efficiency of singlet oxygen sensitization trends with the excited state lifetimes measured by TA. **Ru-phen** through **Ru-1T** had no excited state signal within the detection limit of the TA instrument (~1 ns), and their ${}^{1}O_{2}$ production was negligible as would be expected for extremely rapid excited state deactivation via other nonradiative pathways. The detection of the ${}^{3}IL/{}^{3}ILCT$ state in **Ru-2T** (τ =5.8–7.9×10² ns) coincided with a modest ${}^{1}O_{2}$ quantum yield (Φ_{Δ} =0.06). Much greater ${}^{1}O_{2}$ sensitization was exhibited by **Ru-3T** and **Ru-4T**, Φ_{Δ} =0.60 and 0.65, respectively, the ${}^{3}ILCT$ lifetimes of which were 23–25 and 20–24 μ s. The quantum yields of **Ru-3T** and **Ru-4T** still fall short of those for the analogous complexes with non-methylated phen ancillary ligands

 $(\Phi_{\Delta}=0.88 \text{ and } 0.87, \text{ unpublished results})$ suggesting that these complexes with strain-inducing ligands have competing pathways for excited state relaxation, including ligand loss via the 3MC state. The 1O_2 quantum yields for the strained bis(6,6'-dmb) analogs of **Ru-2T**, **Ru-3T**, and **Ru-4T** were previously determined to be 0.09^a , 0.42, and 0.43, respectively, 78,88 also confirming the abrupt switch in photophysical behavior between n=2 and 3 for related but structurally different ancillary ligands and highlighting the impact of the ancillary ligand identity on the overall properties such as 1O_2 sensitization and ligand dissociation. We have addressed this relationship in more detail elsewhere.

Table 4. Transient Absorption Lifetimes, Singlet Oxygen Quantum Yields, and Photosubstitution Quantum Yields for the Compounds in MeCN at Room Temperature. Excitation wavelengths (nm) for 1O_2 emission are indicated in parentheses. Photosubstitution quantum yields (from the first 5 s) are listed for the compounds in water using broadband visible light (400–700 nm, 20 mW cm⁻²). The samples for photosubstitution were pre-equilibrated for 3 h prior to the experiment.

Cmpd	T _{TA}	$\Phi_{\Delta} (\lambda_{ex} / nm)$	Ф _{PS (5s)}
Ru-phen	_	0.01 (420)	0.0103
Ru-0T	_	0.01 (420)	0.0188
Ru-1T	_	0.01 (420)	0.0197
Ru-2T	5.8–7.9×10 ² ns	0.06 (400)	0.0122
Ru-3T	23–25 µs	0.60 (452)	0.0052
Ru-4T	20–24 µs	0.65 (463)	0.0028

3.3.4 Excited state pathways

The photophysics of Ru(II) polypyridyl complexes has been studied extensively. Ultrafast laser spectroscopy of the archetype $[Ru(bpy)_3]^{2+}$ has revealed that initial excitation to the strong 1MLCT band is followed by highly efficient and rapid ($\tau\approx15$ –40 fs) ISC to the 3MLCT state. ${}^{102-105}$ In the case of $[Ru(bpy)_3]^{2+}$ and many other related complexes, the 3MLCT state is emissive and decays with an time constant of around 1 µs, with inefficient population of the photodissociative 3MC state. The addition of methyl groups at the 6,6'- positions of bpy has the physical effect of introducing steric strain in the inner coordination sphere of Ru(II), which in turn has the electronic effect of lowering the 3MC state by around 0.5 eV to be very close to the 3MLCT state. 106 For example, $[Ru(tmbpy)_3]^{2+}$ (where tmbpy = 4,4',6,6'-tetramethyl-2,2'-bipyridine), the ${}^3MLCT \rightarrow {}^3MC$ conversion occurs within 0.16 ps, followed by relaxation to ground state in 7.5 ps. 106

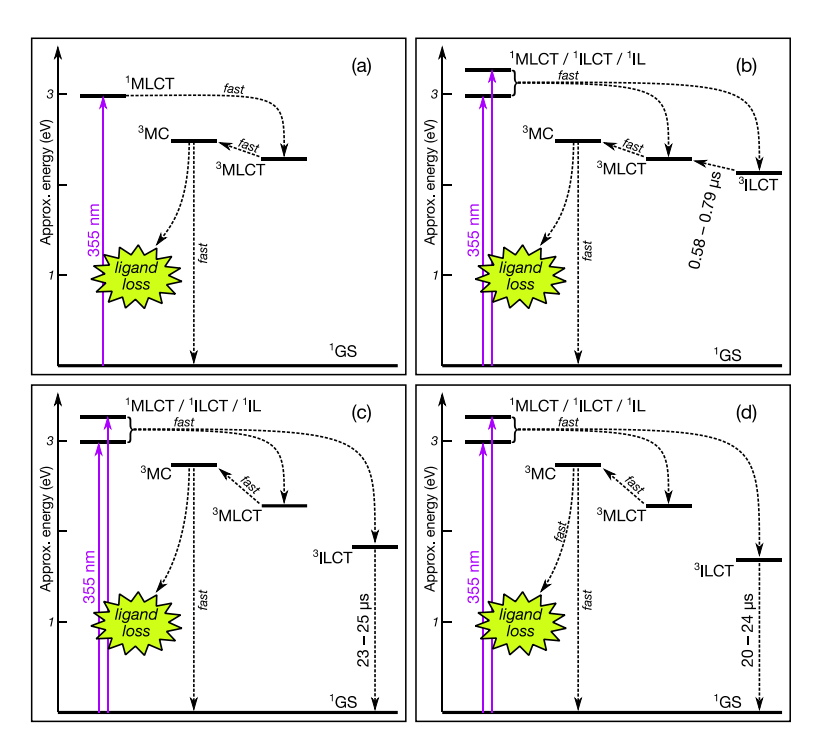
The behavior encountered for compounds in this series lacking thiophenes or having only one thiophene ring is consistent with an accessible ³MC state as depicted in the Jablonski diagram in Scheme 2 and supported by our computational studies. Excitation at 355 nm to form the Frank-Condon ¹MLCT states leads to rapid ISC to the ³MLCT state in the case of **Ru-phen** through **Ru-1T**. The absence of any detectable steady-state ³MLCT emission and no TA signal from this state on the nanosecond timescale for these three compounds suggests an almost barrierless crossover between the ³MLCT and ³MC states. Computation suggests that the energy difference between T₁ (³MLCT) and the lowest-lying ³MC state near 2.5 eV is only about 0.2 eV. Ground

^a Original $Φ_Δ$ value of 0.34 for [Ru(6,6'-dmb)₂(IP-2T)](PF₆)₂ was incorrectly calculated. Reported value 0.09 here was remeasured 4× with fresh 20 μM solutions and excitation at 395 nm.

state recovery then takes place through a nonradiative, nonphotochemical pathway or through ligand dissociation in a timeframe too rapid to be observed with the instrumentation used here.

For Ru-2T–Ru-4T, excitation directly to the 1 ILCT state is possible based on the UV-Vis singlet-singlet absorption transitions. In the proposed model, subsequent ISC populates the long-lived oligothiophene-based 3 ILCT state that was detected as a prominent ESA in the TA spectra and implicated in efficient 1 O₂ production. $^{7,88,90,79,80,96,98,99,107-111}$ While population of the 3 MLCT from the 3 ILCT state could occur, 80,80,112 we were unable to detect any evidence of the 3 MLCT state on the nanosecond to microsecond timescale. However, population of the 3 MLCT state from the initially formed singlet excited states and subsequent crossover to the 3 MC manifold could also explain the absence of a detectable 3 MLCT state for these more π -expanded oligothiophene Ru(II) complexes. The higher 1 O₂ quantum yields for Ru-3T and Ru-4T suggest that competing nonradiative pathways for ground state recovery are slower. By contrast, the relatively low 1 O₂ quantum yield for Ru-2T, despite its 3 ILCT signature in the TA spectrum, suggests that deactivation of the 3 ILCT state might occur via crossover to a near-isoenergetic 3 MLCT state that is in turn rapidly depopulated by the 3 MC state. The computed 3 IL- 3 MLCT energy gap of only about 0.16 eV supports this assertion.

In summary, the proposed model of ${}^3MLCT \rightarrow {}^3MC \rightarrow S_0$ suggests that photodissociation is an important relaxation pathway for **Ru-phen** through **Ru-1T**, while slow ${}^3ILCT \rightarrow S_0$ accounts for the efficient 1O_2 generation by **Ru-3T** and **Ru-4T**. The model for **Ru-2T** involves both of these decay mechanisms, owing to an 3MLCT state in close proximity to the 3ILCT detected by TA. In this case, ${}^3ILCT \rightarrow {}^3MLCT \rightarrow {}^3MC \rightarrow S_0$ could explain the observed 3ILCT transient without a detectable 3MLCT state on the interrogated timescale and the low 1O_2 quantum yield. It should be noted that these interpretations derive from photophysical experimental data analyzed in the context of vertical excitation energies and NTO topologies computed for the Frank-Condon (S_0) and S_0 are structures. To provide a more detailed molecular mechanism of the excited state processes at play, photochemical experiments combined with computational optimization of triplet energy surfaces were carried out to test these preliminary models.



Scheme 2: Simplified Jablonski diagrams depicting the photophysical processes in: (a) **Ru-phen**, **Ru-0T**, and **Ru-1T**, (b) **Ru-2T**, (c) **Ru-3T**, and (d) **Ru-4T**.

3.3.5 Photosubstitution

The complexes were stable in aqueous solution in the dark, but all underwent a similar photosubstitution reaction when irradiated with broadband visible light (400–700 nm, irradiance=20 mW cm⁻²; Figures S39–S53). In all cases, HPLC analysis indicated that visible light caused photoinduced ligand loss of one of the strain-inducing 2,9-dmp ligands. The quantum yields (Φ_{PS}) for this photosubstitution reaction (Table 4) were compared to determine the impact of the spectator IP-*n*T ligand on this process.

The calculated values for Φ_{PS} were less than 2% for all of the compounds, which is in the range measured by others for photosubstitution reactions of distorted Ru(II) complexes. ^{49,52,58,76,113,114} For $n \le 2$ and the complexes lacking thienyl groups, values for Φ_{PS} were higher and fell between 1–2%. Fusing an imidazole group (**Ru-0T**) to phen (**Ru-phen**) increased Φ_{PS} from 1 to 1.8%, and the addition of one thiophene (**Ru-1T**) had almost no effect on Φ_{PS} relative to **Ru-0T**. Within the thienyl family, however, the spectator ligand influenced this process. Values for Φ_{PS} decreased as the number of thiophenes increased, ranging from almost 2% for **Ru-1T** to 0.28% for **Ru-4T**. Notably, both **Ru-3T** and **Ru-4T** were well under 1%. This result parallels what we observed for $[Ru(6,6'-dmb)_2(IP-nT)]Cl_2$ (n=1-3).⁸⁸

Overall, the decreased photosubstitution quantum yields ($\Phi_{PS} \le 0.5\%$) correlated with increased singlet oxygen production (Tables S7 and S8), where **Ru-3T** and **Ru-4T** had the largest singlet oxygen quantum yields ($\Phi_{\Delta} \ge 60\%$) and longest ³ILCT lifetimes ($\tau_{TA} \ge 20 \mu s$). Based on the assumption that photosubstitution involves the ³MC state, these findings support the proposed

model whereby the ³MC state plays a more pronounced role in the excited state relaxation of **Ru-phen** through **Ru-1T** and less so for **Ru-3T** and **Ru-4T**, with intermediate involvement for **Ru-2T**.

3.3.6 Triplet potential energy surfaces and excited-state decay mechanisms

The characterization of potential energy surfaces along reaction coordinates of interest can reveal not only the molecular basis of the operative deactivation mechanisms, but also the intrinsic competition between them. The most relevant triplet potential energy surfaces involving the Ru-N bond elongation that mediates the population of MC states are shown in Figure 7 for **Ru-1T** and **Ru-4T**. These two compounds were selected for the comparison because they exhibit very different photophysical (Φ_{Δ} , τ_{TA}) and photosubstitution (Φ_{PS}) characteristics (Table 4). The excited-state mechanisms available to **Ru-1T** and **Ru-4T** are controlled by electronic states of distinctly different nature, explaining the dramatic differences in their observed excited-state lifetimes and photosubstitution quantum yields.

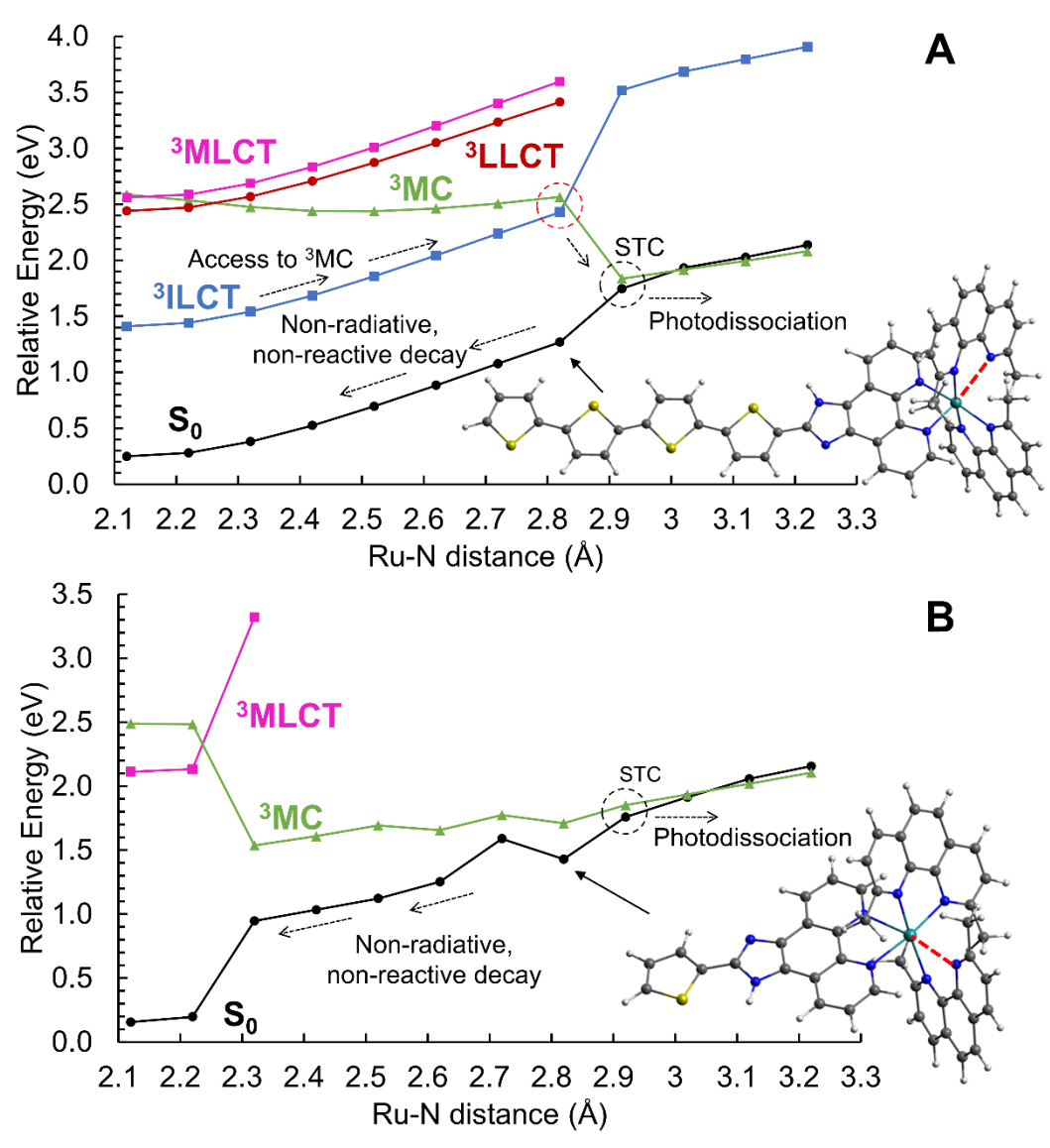


Figure 7. Triplet potential energy surfaces of Ru-4T (A) and Ru-1T (B) obtained by optimizing the T_1 relaxation. Dashed arrows indicate the competing excited-state decay pathways. The 3D representations correspond to a Ru-N distance of 2.82 Å, with the elongated bond highlighted by a dashed red line. The singlet–triplet crossing (STC) points are highlighted with black dashed circles. In panel A, the red dashed circle denotes the energy degeneracy between the 3 ILCT and the 3 MC states of Ru-4T. The excited-state potential energy surfaces were computed at the TD-DFT/M06 level of theory by means of relaxed scan calculations of one Ru-N bond from 2.12 to 3.22 Å. The basis set 6-31+G(d,p) has been used for the C, N, O, and S elements, while the Ru(II) has been described with the Stuttgart-Dresden pseudopotential. A smaller basis set has been employed for the TD-DFT optimizations (Supporting Information)

The lowest-lying triplet state of **Ru-4T** is of ${}^3\text{IL}/{}^3\text{ILCT}$ character at short Ru-N distances (Figure 7A), where the excited state is localized over the oligothiophene chain. Accordingly, molecular motion taking place in the inner coordination sphere of Ru, such as Ru-N elongation, destabilizes both the ${}^3\text{IL}/{}^3\text{ILCT}$ and S₀ curves in a similar manner, increasing their energies in parallel. However, this Ru-N stretching has the opposite effect on the dissociative ${}^3\text{MC}$ state, which evolves over a relatively flat surface with Ru-N bond elongation. The crossing between the ${}^3\text{IL}/{}^3\text{ILCT}$ and ${}^3\text{MC}$ surfaces takes place at a relatively low energy (~2.5 eV) and at a Ru-N

distance of 2.8 Å. The energy degeneracy between the two states allows energy transfer at the surface crossing, but the energy barrier to access this point from the 3 IL/ 3 ILCT triplet minimum, which is close to the Franck-Condon region (minimum Ru-N distance), is estimated to be \sim 1 eV (\sim 96 kJ mol $^{-1}$) and likewise corresponds to the energy required to stretch the Ru-N bond in the ground state. Despite the energy barrier likely being overestimated due to the relaxed scan procedure, it is reasonable to conclude that it is sufficiently high to trap the 3 IL/ 3 ILCT excited state for several tens of microseconds (20–24 μ s, Table 4).

The 3 MC surface crosses the singlet ground state (singlet–triplet crossing, STC) at a Ru-N distance of ~2.9 Å (Figure 7A and S34). Intersystem crossing repopulates the ground state S₀ either through nonradiative decay that does not involve ligand loss or through dissociation of the strain-inducing 2,9-dmp ligand. Return to the Franck-Condon region without ligand loss is barrierless, whereas the latter requires additional energy to break the two Ru-N bonds (in line with its low value for $\Phi_{PS} \approx 0.3\%$).

The profile computed for **Ru-1T** is very different (Figure 7B), owing to the lowest-energy triplet being of ³MLCT character close to the Franck-Condon region. In stark contrast to **Ru-4T**, the surface crossing of the lowest-energy triplet (here ³MLCT) with the ³MC state occurs at a much shorter Ru-N distance (~2.3 Å). Therefore, population of the dissociative ³MC state through internal conversion from ³MLCT is barrierless. The surface of the ³MC state is relatively flat and crosses S₀ at a Ru-N bond distance of ~2.9 Å. Repopulation of the ground state at the surface crossing occurs either without ligand loss (major pathway) or with the loss of one of the 2,9-dmp ligands (minor pathway). This model explains the much shorter excited-state lifetime of **Ru-1T** (within the instrument response function or excitation pulse, <5 ns) that is reminiscent of Fe(II)-based transition metal complexes, with excited-state lifetimes on the order of tens of picoseconds. ^{117,118,115,119}

For **Ru-4T**, the non-radiative decay of the lowest-lying 3 ILCT state, localized exclusively over the thiophene chain, has been studied by optimizing the crossing point between the T_1/S_0 surfaces with the ORCA 4.2 software. 120 The minimum energy crossing point (MECP) is characterized by a bending of the thiophene chain up to 34° as a consequence of the distortion taking place at only one of the thiophene rings, as shown in Figure S35. The geodesic coordinate interpolation 121 between the T_1 equilibrium geometry and the MECP reveals an energy barrier of ${}^{\sim}0.64$ eV (15.8 kcal mol ${}^{-1}$), which is compatible with the 20–24 ${}^{\mu}$ s TA lifetime reported in Table 4 and kinetically faster than the 3 ILCT ${}^{\rightarrow}$ 3MC pathway shown in Figure 7A. It is therefore reasonable to ascribe this mechanism to the 3 ILCT/ 1 GS pathway shown in Scheme 2d.

The computed triplet and ground state surfaces support the photophysical model proposed from the initial computational and photophysical experiments, yet they add an important facet to consider when rationalizing the differences among the series. The Ru-N bond distance at which the 3MC surface crosses the T $_1$ surface (>2.9 Å for Ru-4T and <2.3 Å for Ru-1T) correlates with the trends for Φ_{PS} , Φ_{Δ} , τ_{TA} , whereby the compound with its ${}^3MC/T_1$ crossing at the shortest Ru-N distance (Ru-1T) has the highest photosubstitution quantum yield, the lowest 1O_2 quantum yield, and the shortest T $_1$ lifetime. Access to the ${}^3MLCT/{}^3MC$ crossing is predicted to occur through a single channel from the 1MLCT state for Ru-1T, whereas two routes to the 3MC state are envisioned for Ru-4T. The first involves access to the 3MC state through the 1MLCT state (${}^1MLCT \rightarrow {}^3MLCT \rightarrow {}^3MC$), and the second involves initial population of the 1ILCT state (${}^1ILCT \rightarrow {}^3ILCT \rightarrow {}^3MC$). The ${}^3ILCT/{}^3MC$ crossing occurs at a much longer Ru-N bond distance, while either an ${}^3LLCT/{}^3MC$ or ${}^3MLCT/{}^3MC$ crossing occurs at much shorter Ru-N bond distances.

Possible ³ILCT→³MLCT equilibrations, observed in other bichromophoric Ru(II) complexes, ^{122–125} could also mediate the population of the ³MC state through the ³ILCT→³MLCT→³MC pathway. Although the ³MLCT/³ILCT crossings have not been explicitly characterized in this work, Figure 7 indicates that their relative energies should be high. Our model assumes limited accessibility, and thus relevance, in the excited-state decay. The role of ³ILCT/³MLCT crossings can be safely considered as similar to the ³ILCT/³MC crossings, possibly contributing to the ultimate population of the ³MC state. Regardless, there is likely a preference for non-reactive relaxation back to the Franck-Condon area (Figure 7), reflected in the small photosubstitution quantum yields in general, because photosubstitution requires additional energy and cleavage of the second Ru-N bond. This model could be an important new insight into the design of dual-action PCT agents but requires further computational and experimental scrutiny (including fs-TA analyses) to understand whether it can be used as a predictive tool.

3.4 Normoxia Studies

3.4.1 Normoxic cellular assay

Ru-phen–Ru-4T were screened for their dark and light cytotoxicities toward SK-MEL-28 human melanoma cells in normoxia. The compounds were generally soluble in high ionic strength DPBS below 50 μ M, but the IP-nT complexes produced suspensions at higher concentrations. Reference **Ru-phen** was fully soluble at all the tested concentrations.

For the cytotoxicity determination, cells growing in log phase were seeded in well plates and allowed to incubate for 2–3 h before dosing with compound (1 nM to 300 μ M). The treated cells were then incubated overnight (~20 h) before measuring cell viability using the resazurin assay for detecting metabolic activity. The photocytotoxicity assay followed a similar protocol except that a light treatment was delivered after PS addition with a drug-to-light interval (DLI) of 14–18 h. EC50 values, the effective concentration to reduce relative cell viability by 50%, were obtained from logistic fits of the dose-response curves for the dark and light conditions. Phototherapeutic indices (PIs) were calculated as the ratio of dark to light EC50 values and reflect amplification of cytotoxic effects by light. The tested PS concentration range was expanded to include concentrations down to 1×10⁻¹⁴ μ M for **Ru-3T** and **Ru-4T** in order to quantify the EC50 values for these more potent PSs.

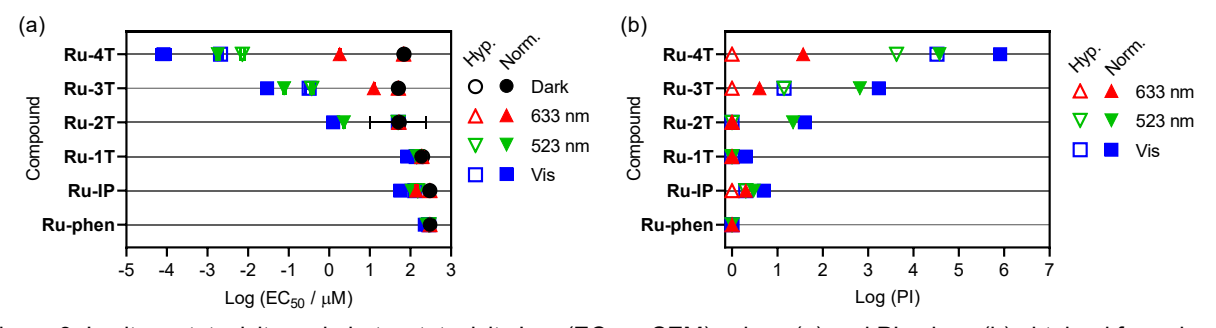


Figure 8. In vitro cytotoxicity and photocytotoxicity Log (EC $_{50}$ ± SEM) values (a) and PI values (b) obtained from dose-response curves in the SK-MEL-28 melanoma cell line with **Ru-phen–Ru-4T**. Treatments included dark (0 J cm $^{-2}$; black circles) and 100 J cm $^{-2}$ doses of 633 nm (red triangles), 523 nm (green inverted triangles), and visible (400–700 nm, blue squares) light. Hypoxic (1% O₂) results are shown with open symbols while normoxic (~18.5% O₂) data are shown with closed symbols.

3.4.2 Dark cytotoxicity in normoxia

The strained complexes were either nontoxic or exhibited low cytotoxicity in the dark. The reference compounds **Ru-phen** and **Ru-0T** ($EC_{50}>300~\mu\text{M}$), lacking thiophene rings, and **Ru-1T** ($EC_{50}=185~\mu\text{M}$) were nontoxic to cells in the absence of a light trigger. **Ru-2T–Ru-4T** had lower EC_{50} values (49.8–67.6 μ M) by comparison, but were still considered relatively nontoxic. The least cytotoxic of the complexes with n=2-4 was **Ru-4T**, with $EC_{50}=67.6~\mu\text{M}$. The uncomplexed 2,9-dmp ligand was also assayed since it could (potentially) act as the cytotoxic agent upon photodissociation from the metal complex. Under our assay conditions, the free ligand showed no cytotoxicity ($EC_{50}>300~\mu\text{M}$).

3.4.3 Photocytotoxicity in normoxia

The photocytotoxicities of the complexes were measured using a fluence of 100 J cm $^{-2}$ and irradiance of 18–22 mW cm $^{-2}$ delivered from broadband visible (450 nm maximum, 400–700 nm) light source or LEDs emitting green (523 nm) or red (633 nm) light. The spectral output of these light sources is shown in Figure S54. For photoactive compounds, activity in normoxia increased with photon energy, with broadband visible light (enriched in the blue wavelengths) producing the most potent phototoxic effects. **Ru-phen**, **Ru-0T**, and **Ru-1T** exhibited minimal cytotoxicity following light activation (Figure 8a, Table S10). Their light EC₅₀ values were similar to their dark values regardless of the light treatment, ranging from 56.5 to 224 μ M with visible light.

As previously reported for related Ru(II) and Os(II) complexes, 79,80,88,96,99 notable photocytotoxic effects began to manifest at n=2. For this strained Ru(II) family, they ranged from single-digit micromolar to picomolar as the number of thiophenes increased. Visible EC₅₀ values were 1.25 μ M for **Ru-2T**, 29.4 nM for **Ru-3T**, and 82.4 pM for **Ru-4T**. The photocytotoxicities were still high, single-digit micromolar to nanomolar, with lower photon energy green light, where EC₅₀ values were 2.30 μ M, 77.1 nM, and 1.79 nM for **Ru-2T**, **Ru-3T**, and **Ru-4T**, respectively.

Although the molar extinction coefficients at 633 nm were vanishingly small (ϵ_{633} =<50 M⁻¹ cm⁻¹), **Ru-4T** still maintained single-digit photocytotoxicity with EC₅₀=1.80 µM. The fact that **Ru-2T** was slightly less absorptive than **Ru-4T** (Figure S55, Table S9) despite its red EC₅₀ value being almost 30-fold less active (EC₅₀=50.3 µM), suggests that 633-nm excitation of **Ru-4T** populates an excited state not available to **Ru-2T** (and less available for **Ru-3T**), underscoring that photocytotoxicity is not determined solely by the number of photons absorbed. We have previously demonstrated that this "red PDT effect" stems from direct excitation to low-lying ³IL states that are extremely potent $^{1}O_{2}$ generators despite the low oscillator strengths associated with spin-forbidden transitions. 7,96,98,110

3.4.4 Phototherapeutic index (PI) in normoxia

The photocytotoxicity, quantified as the light EC $_{50}$ value, reflects the combined cytotoxic effects of both the dark and light conditions whereas the PI represents the amplification of these cytotoxic effects with light and is the appropriate parameter to use for comparing PS potencies and discerning wavelength dependencies (Figure 8b). Regardless of the light treatment, the normoxic PI values for **Ru-phen**, **Ru-OT**, and **Ru-1T** were <5, with **Ru-phen** being essentially inactive (PI=~1). The very marginal PIs are consistent with what has been observed for strained Ru(II) complexes with low-lying 3 MC states and inaccessible 3 IL/ 3 ILCT states, resulting in very poor 1 O $_2$ quantum yields.

The TA experiments and computational studies revealed that the ${}^{3}IL/{}^{3}ILCT$ becomes accessible at n=2, although the triplet lifetime was still relatively short ($\tau_{TA}<1~\mu s$) and ${}^{1}O_{2}$ quantum

yield low (Φ_{Δ} =6%) for **Ru-2T** due to the presence of a competing low-lying ³MC state. This was reflected in the moderate activity of **Ru-2T**, where visible and green light gave PIs of 40 and 22, respectively, and red light was ineffective.

The effect of additional thiophenes beyond n=2 was dramatic. The inaccessible ${}^{3}MC$ state in **Ru-3T** and **Ru-4T** resulted in much longer triplet state lifetimes (τ_{TA} =20–25 μ s) and much higher ${}^{1}O_{2}$ quantum yields (Φ_{Δ} =60–65%), which profoundly impacted the PIs. The additional thiophene ring in **Ru-3T** increased the PI_{vis} to ~1700, whereas four thiophenes in **Ru-4T** resulted in a PI_{vis} of 8.2×10⁵, a roughly 500-fold improvement over **Ru-3T** and 10⁴-fold improvement over **Ru-2T**. **Ru-3T** and **Ru-4T** were also highly active with lower photon energy green light (PI_{green}=658 and 38,000, respectively), but less active with red (PI_{red}=4 and 38, respectively).

This wavelength dependence for the PI, which was much more pronounced for **Ru-4T**, was not solely due to differences in the numbers of absorbed photons under the three different light conditions. Considering absorption by **Ru-4T** over the full peak areas for the light sources used (rather than at single wavelengths), there was only a 16-fold difference in absorbed photons between the visible and red condition and no difference between the visible and green (Table S9), yet the PIs differed by over 2×10⁴- and 22-fold, respectively. For **Ru-3T** these PIs differed by 430-and ~3-fold, respectively. Assuming that the differences in the PIs are not due to differences in the numbers of absorbed photons between the cell-free solution and the cellular environment at the time of irradiation, the photophysical trajectory from the initially populated state(s) clearly plays a role in the efficiencies with which certain reactive excited states are populated. It is possible that different mechanisms for photocytotoxicity may be invoked by different wavelengths. The photophysical dynamics of **Ru-4T** proved to be more sensitive to these factors.

Both **Ru-3T** and **Ru-4T** were extremely potent with visible and green light but exhibited a stark contrast in activity despite similar T_1 excited state configurations and lifetimes, 3MC energies, quantum yields for photosubstitution (Φ_{PS} =0.52% for **Ru-3T** versus 0.28% for **Ru-4T**) and 1O_2 production (Φ_{Δ} =60% for **Ru-3T** versus 65% for **Ru-4T**), and numbers of absorbed photons (6.14 ×10⁻⁵ for **Ru-3T** versus 10.9×10⁻⁵ mol m⁻² s⁻¹ for **Ru-4T**). However, the two compounds differed in their 3ILCT -based T_1 energies (1.87 eV for **Ru-3T** versus 1.71 eV for **Ru-4T**) as well as the presence of a second higher-lying 3ILCT state (T_2) for **Ru-4T** that was of similar energy as the lowest-lying 3MLCT states. The less accessible 3MC states and the larger 3ILCT - 3MLCT energy gap for **Ru-4T** along with the presence of a second 3ILCT state may contribute to the superior activity of **Ru-4T** over **Ru-3T** as well as the pronounced wavelength dependence for the PIs.

The fact that the PIs were largest for the two compounds with the lowest photosubstitution quantum yields and highest-lying 3MC states suggests that photosubstitution is not an important excited state decay pathway contributing to the photocytotoxicities exhibited by **Ru-3T** and **Ru-4T**. Sensitization of 1O_2 may be the source of photocytotoxicity, but the values for Φ_Δ were very similar for the two compounds despite drastically different photocytotoxicities. Also, the 1O_2 quantum yields were significantly lower than those measured for some of our best 1O_2 generators (under cell-free conditions) yet the activity of **Ru-4T** was much greater under identical assay conditions. Nevertheless, their intracellular sensitivities to and interactions with excited state quenchers, including oxygen, could be different. Therefore, the source of photocytotoxic effects is not entirely captured in the cell-free 1O_2 quantum yield measurement.

3.5 Hypoxic Studies

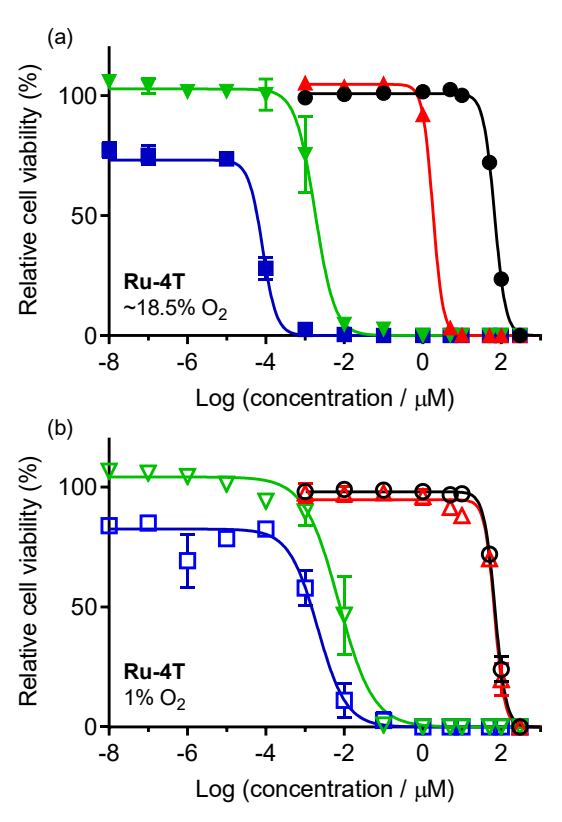


Figure 9. Dose-response (±SD) of **Ru-4T** in (a) normoxic ~18.5% O₂ or (b) hypoxic 1% O₂ treated SK-MEL-28 melanoma cells. Treatments included dark (0 J cm⁻²; black circles) and 100 J cm⁻² doses of 633 nm (red triangles), 523 nm (green inverted triangles), and visible (400–700 nm, blue squares) light.

Ru-phen–Ru-4T were further tested for their (photo)cytotoxic effects in hypoxia (1% O₂) as described for normoxia, with both dark and light treatments, except that the plates to be light treated were equilibrated in hypoxia and sealed with highly transparent, low gas permeable qPCR film after the cells were dosed with compound but prior to illumination outside the hypoxia chamber. Establishment of low oxygen tension and maintenance at the time of illumination is critical for assessing hypoxic activity. We previously showed this method using special qPCR films accommodates illumination times up to 1.5 h outside of the hypoxia chamber. ^{76,79,80} [Ru(bpy)₂(dppn)]Cl₂, an oxygen-dependent PS, was used as an internal control for confirming that hypoxia was maintained. Following treatment with the same light parameters used in normoxia, the films were removed, and both dark- and light-treated plates were returned to a normoxic incubator for ~20 h before assaying cell viability using resazurin. We previously established ^{76,79,80} that the recovery period in normoxia is required for the resazurin indicator to function properly.

3.5.1 Photocytotoxicities and Pls in hypoxia (1% O₂)

As observed for normoxia, **Ru-phen–Ru-1T** also lacked photocytotoxic effects in hypoxia (1% O₂). Their dark and light EC₅₀ values were 50 µM or greater and their PIs were close to 1 (Figure 8a, Table S10). **Ru-2T** was also inactive in hypoxia despite having single digit micromolar

photocytotoxicity and PIs of 40 and 22 in normoxia with visible and green light, respectively. In hypoxia, the light EC₅₀ values for **Ru-2T** increased to around 50 μ M to afford PIs of exactly 1 regardless of the light condition. This was also true for **Ru-3T** and **Ru-4T** with red light, where red EC₅₀ values were within 3% of dark EC₅₀ values.

Compounds **Ru-3T** and **Ru-4T**, however, maintained excellent photocytotoxic profiles in the much more challenging hypoxic environment with visible and green light. Their photocytotoxicities were attenuated compared to normoxia, but **Ru-3T** still displayed submicromolar activity (visible EC_{50} =320 nM, green EC_{50} =370 nM) and **Ru-4T** was single-digit nanomolar (visible EC_{50} =2.09 nM, green EC_{50} =7.20 nM). The corresponding PIs in hypoxia for **Ru-3T** were >100 (PI_{green}=136 and PI_{vis}=158), which are unprecedented. Remarkably, **Ru-4T** had even larger PIs in hypoxia. Values for PI_{green} and PI_{vis} were approximately 9,700 and 33,000, respectively, which are the largest hypoxic PIs reported to date by over two to three orders of magnitude. The photocytotoxic responses elicited by **Ru-4T** toward SKMEL28 cells under both oxygen conditions with the different light parameters are compared in Figure 9.

The wavelength dependence observed for these PIs in normoxia was attenuated in hypoxia (Figure 8b). There was almost no difference in PI_{green} and PI_{vis} for **Ru-3T** in hypoxia versus a >2.5-fold difference in normoxia. For **Ru-4T**, there was ~3.5-fold difference in PI_{green} and PI_{vis} in hypoxia versus a 22-fold difference in normoxia. We propose that there could be a wavelength- and oxygen-dependence to the excited state partitioning that could in turn influence the photocytotoxic pathways, but this has not been substantiated.

Notably, the compounds with the poorest photosubstitution quantum yields (0.27% for **Ru-4T** and 0.50% for **Ru-3T**) were the only compounds that were active in hypoxia. Minimizing access to the ³MC state in compounds having accessible ³IL/³ILCT states produced *better* activity under both hypoxic (1% O₂) and normoxic (~18.5% O₂) conditions as illustrated in Figure S58. This observation is the opposite of what would be expected if the photodissociative ³MC state were responsible for the photocytotoxic mechanism in hypoxia. From this we conclude that the nondissociative ³ILCT state is responsible for the ultra-potent activity and is superior to the ³MC state for eliciting a hypoxic response in this compound class.

3.6 Validation of Ru-3T and Ru-4T Activity

A longitudinal study (repeat 1–5, Figure 10) was undertaken to validate the unprecedented EC_{50} values and PIs obtained in normoxia and hypoxia for **Ru-3T** and **Ru-4T** (initial result=repeat 0, Figure 8). The study intentionally varied some of the assay parameters that commonly differ (but can be controlled) across laboratories (Figure S56, Tables S11–14): (i) plate mapping, (ii) pipette tip consumables, and (iii) cell seed stocks. These variations are described in more detail under methods. Otherwise, all cells were used within the same passage number (10–15), and all assays used the same lot numbers for consumables (media, serum, solvents, plastics) and same batch of PS. Each repeat was performed in triplicate.

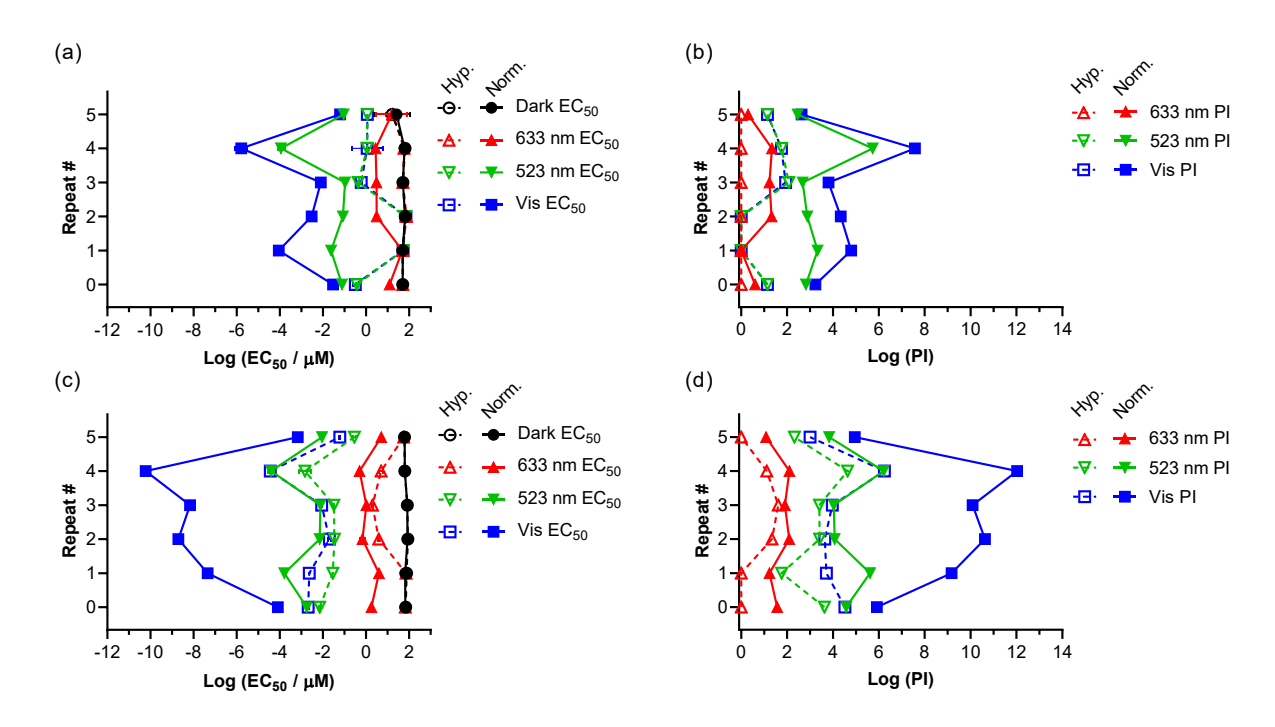


Figure 10. Interassay performance with various factors changed across each repeat as described in the experimental section. Cytotoxicity and photocytotoxicity of **Ru-3T** (top, a+b) and **Ru-4T** (bottom, c+d) in normoxic- (filled symbols, solid lines; \sim 18.5% O_2) and hypoxic-treated (open symbols, dashed lines; 1% O_2) SK-MEL-28 melanoma cells. Log (EC₅₀ ± SEM) values (left) and PI values (right). Treatments included dark (0 J cm⁻²) and 100 J cm⁻² doses of 633 nm, 523 nm, and visible (400–700 nm) light.

The dark cytotoxicities for the two compounds were similar and consistent across the longitudinal repeats under both normoxia and hypoxia, with mean dark EC $_{50}$ values for **Ru-3T** and **Ru-4T** of 50.5 and 72.7 μ M, respectively. While their photocytotoxicities did vary, the high potencies of both **Ru-3T** and **Ru-4T** were reproducible and, in some cases, exceedingly greater than the initial result (repeat 0) under both normoxic and hypoxic conditions.

While both compounds were excellent normoxic PSs with visible light, **Ru-3T** was less potent than **Ru-4T** in normoxia and considerably less robust and potent under hypoxia. Over the six separate experiments, each performed in triplicate, visible EC₅₀ values for **Ru-3T** ranged from 1.6×10^{-6} to 6.2×10^{-2} µM in normoxia. Values for normoxic Pl_{vis} ranged from 10^2 to 10^7 . In hypoxia, the EC₅₀ values were lower with larger variation and ranged from 0.32 to 72 µM. The Pl_{vis} in hypoxia ranged from 1-158.

Ru-4T was a much more consistent top performer under both oxygen conditions, with photocytotoxicity reaching attomolar levels with visible light in normoxia. EC₅₀ values ranged from 6.0×10^{-11} to 6.9×10^{-4} µM and values for Pl_{vis} ranged from $\sim 10^5$ to 10^{12} . While the mean photocytotoxicity was picomolar, three out of six separate experiments gave femtomolar activity and one even attomolar. In hypoxia, **Ru-4T** was active at picomolar levels with visible light, with EC₅₀ values ranging from 3.7×10^{-5} to 6.2×10^{-2} µM and values for Pl_{vis} ranging from 10^3 to 10^6 . To the best of our knowledge, no comparable activity has been reported in hypoxia or normoxia.

Ru-3T and **Ru-4T** were also extremely active with green light and followed the trends highlighted for visible light whereby **Ru-3T** was of lower potency with a higher variation in activity, especially in hypoxia. The range of EC₅₀ and Pl₅₂₃ values for the six separate experiments performed in triplicate are listed in Tables S11–14 for both compounds and both oxygen conditions. The normoxic EC₅₀ and Pl values for **Ru-3T** with green light ranged from 1.1×10^{-4} to 1.1×10^{-1} µM and 2.9×10^{2} to 5.4×10^{5} , respectively. The corresponding values in hypoxia ranged from 4.0×10^{-5} to 9.2×10^{-3} µM and 4.0×10^{-5} to 4.0×10^{-5} t

As observed for the initial experiment (repeat 0), **Ru-3T** and **Ru-4T** were generally less active with red light in normoxia, although manipulating experimental variables across repeats 1–5 led to improved activity in some cases. **Ru-3T** was inactive with red light in hypoxia. The values for EC₅₀ and Pl₆₃₃ for **Ru-3T** ranged from 2.8 to 49 μ M and 1 to 22 in normoxia, while those for **Ru-4T** ranged from 0.51 to 5.2 μ M and 12 to 130. Despite minimal absorption at 633 nm and attenuated normoxic activity, the EC₅₀ and Pl₆₃₃ values for **Ru-4T** were still as low as 2.0 μ M and as high as 41, respectively.

Given that greater activity in general led to a more robust performance under the more challenging hypoxic condition, it was not surprising that the treatment of **Ru-4T** with red light in hypoxia or any light treatment of **Ru-3T** in hypoxia yielded much more variation in the observed activities across the six repeats that changed certain variables. This is exemplified by **Ru-4T** with red light, where normoxic EC $_{50}$ values covered a relatively narrow range of 0.51 to 5.2 μ M and hypoxic values covered a much wider range at 2.0–72 μ M in hypoxia. The wide activity range in hypoxia was attributed to a combination of the purposely varied parameters as well as slight differences in oxygen tension that would be expected when relying on passive gas exchange to achieve 1% hypoxia.

In summary, the main purpose of the longitudinal study was to verify the unprecedented activities of Ru-3T and Ru-4T using controllable variables that might simulate expected differences across different laboratories performing similar experiments. We also verified the wavelength dependence for each oxygen condition and the difference in this dependence between normoxia and hypoxia. It was found that the most active compound, Ru-4T, was a much more consistent top performer across all conditions, demonstrating that the extremely high potency initially observed with visible light in normoxia was a reliable predictor of relative activity under the most challenging conditions.

The combination of **Ru-4T** and visible or green light consistently yielded unprecedented potencies in both normoxia ($Pl_{vis}=10^5-10^{12}$) and in hypoxia ($Pl_{vis}=10^3-10^6$), reaching femtomolar levels in normoxia and picomolar activity in hypoxia – making **Ru-4T** the most potent PS reported to date. Even with red light, the mean PI values were among some of the largest reported values for hypoxia^{75,76} prior to our more recent benchmark of 71 for red light with an Os(II)-based photosensitizer.⁷⁹ Up to that point, PIs in hypoxia with any wavelength of light had not even reached 10^2 .

The longitudinal study also supported the assertion that the photocytotoxic pathways may not only change between wavelengths but also between oxygen conditions. Over six separate experiments run in triplicate, the data support a mechanism for both **Ru-3T** and **Ru-4T** with visible

light in normoxia that is distinct from that of the other wavelengths and oxygen condition and subject to higher variability.

3.7 Maximum tolerated dose (MTD) in mice

Given that **Ru-3T** and especially **Ru-4T** emerged as leads from this study, their general toxicities toward female C57BL/6J mice when injected either intraperitoneally (IP) or intravenously (IV) were assessed to determine whether these compounds should advance to in vivo evaluation. The mice were treated with **Ru-3T** and **Ru-4T** at doses of 25, 50, 100, 150, and 200 mg kg⁻¹ delivered by IP injection. No dose-limiting toxicity was observed even at the highest dose. The mice were responsive and alert at all times but appeared somewhat subdued and transiently hunched after injection, which resolved completely within 2–3 h for **Ru-4T**. For **Ru-3T**, there were no symptoms at all with the 25 mg kg⁻¹ dose. The intermediate doses produced mild symptoms that resolved within 6 h, but the highest dose (200 mg kg⁻¹) produced mild symptoms that did not resolve over the study period. With no weight loss and no signs of moderate toxicity over the two-week study for either compound, the IP MTD was estimated to be ≥200 mg kg⁻¹ for both PSs.

Both **Ru-3T** and **Ru-4T** were well tolerated at IV doses of 12.5 and 25 mg kg⁻¹ with no symptoms and no weight loss but resulted in death at 50 mg kg⁻¹. Therefore, the IV MTD for both compounds was estimated to be less than 50 mg kg⁻¹ but higher than 25 mg kg⁻¹. The reduced MTD with IV injection compared to IP injection is in agreement with what is generally observed, and the values obtained are guiding current in vivo antitumor experiments.

4. CONCLUSIONS

Complexes in the **Ru-phen–Ru-4T** family were explored to determine whether they act as dual-action PDT/PCT agents by specific manipulation of key excited states, 3MC and ${}^3IL/{}^3ILCT$ states, as determined by the coordinated ligand(s). The IP-nT ligands controlled access to ${}^3IL/{}^3ILCT$ states, whereas the 2,9-dmp ligands provided the necessary strain for access to photodissociative 3MC states. Systematic variation of both singlet and triplet IL/ILCT energies through thiophene chain extension was supported by both computation and spectroscopy. At one extreme, the 3IL energies were too high to be accessible (**Ru-phen** through **Ru-1T**), leaving the predominant decay pathways as photodissociation and/or nonradiative thermal relaxation back to the ground state through the ${}^3MLCT \rightarrow {}^3MC \rightarrow S_0$ trajectory. At the other extreme, the 3IL state was better described as mixed ${}^3IL/{}^3ILCT$ and was substantially lower in energy than the lowest-lying 3MLCT state, whereby excited state relaxation occurred primarily through the ${}^3ILCT \rightarrow S_0$ channel with efficient 1O_2 production for **Ru-3T** and **Ru-4T**. The model for **Ru-2T** fell in between these two extremes due to an ${}^3IL/{}^3ILCT$ state in close proximity to its 3MLCT state, where ${}^3ILCT \rightarrow {}^3MC \rightarrow S_0$ and ${}^3MLCT \rightarrow {}^3MC \rightarrow S_0$ deactivation pathways may both contribute to the observed photophysics.

Optimization of the **Ru-1T** and **Ru-4T** triplet energy surfaces as a function of the Ru-N bond distance revealed that the 3MC surface crosses the T₁ surface at >2.9 Å for **Ru-4T** and <2.3 Å for **Ru-1T**. This finding paralleled the trends for Φ_{PS} , Φ_{Δ} , and τ_{TA} , whereby the compound with its 3MC -T₁ crossing at the shortest Ru-N distance (**Ru-1T**) had the highest photosubstitution quantum yield, the lowest 1O_2 quantum yield, and the shortest T₁ lifetime. The 3MLCT - 3MC crossing was the only accessible triplet-triplet crossing for **Ru-1T**, whereas **Ru-4T** had several crossings: 3LLCT - 3MC and 3MLCT - 3MC crossings at shorter Ru-N bond distances and an 3ILCT - 3MC crossing at a much longer Ru-N bond distance. The fact that the ${}^3IL/{}^3ILCT$ state was unequivocally the lowest energy excited state in the Frank-Condon region and for Ru-N bond distances up to

2.8 Å provides some rationale as to why **Ru-4T** had a lower photosubstitution quantum yield, a much larger ${}^{1}O_{2}$ quantum yield, and a much longer T_{1} lifetime by comparison. The conclusion was that the excited state dynamics of **Ru-1T** were governed in large part by the ${}^{3}MC$ state and by the ${}^{3}IL/{}^{3}ILCT$ state for **Ru-4T**. This distinction afforded the opportunity to assess which state was more important for photocytotoxicity in normoxia and in hypoxia.

The ³ILCT states associated with Ru-3T and especially Ru-4T were superior for photocytotoxicity in normoxia, where ¹O₂ would be expected to be the prime mediator. These compounds were also the only compounds that were active in hypoxia despite having the poorest photosubstitution quantum yields. The observation that *minimizing* photosubstitution in this family actually produced better activity under both hypoxic and normoxic conditions led us to conclude that Ru-4T and Ru-3T do not act as dual-action PDT/PCT agents and that the exceptional potency of these metal complexes is most likely due to catalytic photosensitization involving ROS and redox pathways that may or may not involve oxygen. Interestingly, the ¹O₂ quantum yields for Ru-3T and Ru-4T were significantly lower than those measured for some of our best 1O2 generators (under cell-free conditions) yet the activity of Ru-4T was much greater. This underscores that the cell-free ¹O₂ quantum yield measurement is not an accurate predictor of the photocytotoxic response and that in this case other complementary pathways are probably involved. Oligothiophenes are known for their complex redox behavior that may contribute to extremely potent oligothienyl-based 3ILCT states. Studies are currently underway to examine these pathways and better understand the differences in potency among Ru-4T and its other [Ru(NN)₂(IP-4T)]Cl₂ analogs and to define the multiple mechanisms that are certainly at play in these systems.

5. ASSOCIATED CONTENT

Synthetic characterization (1D and 2D NMR, HPLC, HRMS), computational details and additional results, spectroscopic characterization (emission, TA), and (photo)biological data are included in the Supporting Information. This material is available free of charge via the Internet at http://pubs.acs.org.

5.1 Author Information

5.1.1 Corresponding authors

M.E.A. <marta.alberto@unical.it> ORCID 0000-0001-9925-7233

C.G.C <colin.cameron@uta.edu> ORCID 0000-0003-0978-0894

S.A.M. <sherri.mcfarland@uta.edu> ORCID 0000-0002-8028-5055

5.1.2 Present address

*J.A.R., L.M.L.: University of North Carolina at Chapel Hill, Chapel Hill, NC, 27599.

\$P.C.B.: Virginia Polytechnic Institute and State University, Roanoke, VA, 24016.

†R.O.H.: Wake Forest University School of Medicine, 307 Winston-Salem, NC 27109, USA

5.1.3 Notes

S.A.M. has a potential research conflict of interest due to a financial interest with Theralase Technologies, Inc. and PhotoDynamic, Inc. A management plan has been created to preserve objectivity in research in accordance with UTA policy.

5.2 Acknowledgements

S.A.M. and C.G.C. thank the National Cancer Institute (NCI) of the National Institutes of Health (NIH) (Award R01CA222227) for support. The content in this work is solely the responsibility of the authors and does not necessarily represent the official views of the National Institutes of Health. S.A.M. and C.G.C. also thank the National Science Foundation (award 2102459) for partial support of this work. S.A.M. also thanks Dr. Daniel Todd as UNCG's Triad Mass Spectrometry Facility manager and his assistants Jennifer Simpson and Diane Wallace. S.A.M. likewise thanks Dr. Franklin Moy for his experimental support and instrument maintenance as UNCG's NMR facility manager. M.E.A. acknowledges the CINECA award under the ISCRA initiative, for the availability of high-performance computing resources and support. A.F.-M. is grateful to Generalitat Valenciana and the European Social Fund (contract APOSTD/2019/149 and project GV/2020/226) for financial support. Part of the calculations have been performed on the LPCT local computing cluster at the Université de Lorraine (France) and at the Tirant III cluster of the Servei d'Informàtica (Universitat de València, Spain).

6. REFERENCES

(1) Sung, H.; Ferlay, J.; Siegel, R. L.; Laversanne, M.; Soerjomataram, I.; Jemal, A.; Bray, F. Global Cancer Statistics 2020: GLOBOCAN Estimates of Incidence and Mortality Worldwide for 36 Cancers in 185 Countries. *CA. Cancer J. Clin.* **2021**, *71* (3), 209–249. https://doi.org/10.3322/caac.21660.

- (2) Celli, J. P.; Spring, B. Q.; Rizvi, I.; Evans, C. L.; Samkoe, K. S.; Verma, S.; Pogue, B. W.; Hasan, T. Imaging and Photodynamic Therapy: Mechanisms, Monitoring, and Optimization. *Chem. Rev.* **2010**, *110* (5), 2795–2838. https://doi.org/10.1021/cr900300p.
- (3) Shafirstein, G.; Bellnier, D.; Oakley, E.; Hamilton, S.; Potasek, M.; Beeson, K.; Parilov, E. Interstitial Photodynamic Therapy—A Focused Review. *Cancers* **2017**, *9* (2). https://doi.org/10.3390/cancers9020012.
- (4) Ahn, P. H.; Finlay, J. C.; Gallagher-Colombo, S. M.; Quon, H.; O'Malley, B. W.; Weinstein, G. S.; Chalian, A.; Malloy, K.; Sollecito, T.; Greenberg, M.; Simone, C. B.; McNulty, S.; Lin, A.; Zhu, T. C.; Livolsi, V.; Feldman, M.; Mick, R.; Cengel, K. A.; Busch, T. M. Lesion Oxygenation Associates with Clinical Outcomes in Premalignant and Early Stage Head and Neck Tumors Treated on a Phase 1 Trial of Photodynamic Therapy. *Photodiagnosis Photodyn. Ther.* 2018, 21, 28–35. https://doi.org/10.1016/j.pdpdt.2017.10.015.
- (5) Rice, S. R.; Li, Y. R.; Busch, T. M.; Kim, M. M.; McNulty, S.; Dimofte, A.; Zhu, T. C.; Cengel, K. A.; Simone, C. B. A Novel Prospective Study Assessing the Combination of Photodynamic Therapy and Proton Radiation Therapy: Safety and Outcomes When Treating Malignant Pleural Mesothelioma. *Photochem. Photobiol.* **2019**, *95* (1), 411–418. https://doi.org/10.1111/php.13065.
- (6) Bulin, A.-L.; Broekgaarden, M.; Simeone, D.; Hasan, T. Low Dose Photodynamic Therapy Harmonizes with Radiation Therapy to Induce Beneficial Effects on Pancreatic Heterocellular Spheroids. *Oncotarget* **2019**, *10* (27), 2625–2643. https://doi.org/10.18632/oncotarget.26780.
- (7) Monro, S.; Colón, K. L.; Yin, H.; Roque, J.; Konda, P.; Gujar, S.; Thummel, R. P.; Lilge, L.; Cameron, C. G.; McFarland, S. A. Transition Metal Complexes and Photodynamic Therapy from a Tumor-Centered Approach: Challenges, Opportunities, and Highlights from the Development of TLD1433. *Chem. Rev.* 2019, 119 (2), 797–828. https://doi.org/10.1021/acs.chemrev.8b00211.
- (8) Chamberlain, S.; Cole, H. D.; Roque, J.; Bellnier, D.; McFarland, S. A.; Shafirstein, G. TLD1433-Mediated Photodynamic Therapy with an Optical Surface Applicator in the Treatment of Lung Cancer Cells In Vitro. *Pharmaceuticals* **2020**, *13* (7), 137. https://doi.org/10.3390/ph13070137.
- (9) De Silva, P.; Saad, M. A.; Thomsen, H. C.; Bano, S.; Ashraf, S.; Hasan, T. Photodynamic Therapy, Priming and Optical Imaging: Potential Co-Conspirators in Treatment Design and Optimization a Thomas Dougherty Award for Excellence in PDT Paper. *J. Porphyr. Phthalocyanines* **2020**, *24* (11n12), 1320–1360. https://doi.org/10.1142/S1088424620300098.
- (10) Henderson, B. W.; Gollnick, S. O.; Snyder, J. W.; Busch, T. M.; Kousis, P. C.; Cheney, R. T.; Morgan, J. Choice of Oxygen-Conserving Treatment Regimen Determines the Inflammatory Response and Outcome of Photodynamic Therapy of Tumors. *Cancer Res.* **2004**, *64* (6), 2120–2126. https://doi.org/10.1158/0008-5472.CAN-03-3513.
- (11) Gollnick, S. O.; Vaughan, L.; Henderson, B. W. Generation of Effective Antitumor Vaccines Using Photodynamic Therapy. *Cancer Res.* **2002**, *62* (6), 1604–1608.
- (12) Castano, A. P.; Mroz, P.; Hamblin, M. R. Photodynamic Therapy and Anti-Tumour Immunity. *Nat. Rev. Cancer* **2006**, *6* (7), 535–545. https://doi.org/10.1038/nrc1894.
- (13) Gollnick, S. O.; Brackett, C. M. Enhancement of Anti-Tumor Immunity by Photodynamic Therapy. *Immunol. Res.* **2010**, *46* (1–3), 216–226. https://doi.org/10.1007/s12026-009-8119-4.
- (14) Gollnick, S. O. Photodynamic Therapy and Antitumor Immunity. *J. Natl. Compr. Cancer Netw. JNCCN* **2012**, *10 Suppl* 2, S40-43. https://doi.org/10.6004/jnccn.2012.0173.
- (15) Reginato, E. Immune Response after Photodynamic Therapy Increases Anti-Cancer and Anti-Bacterial Effects. *World J. Immunol.* **2014**, *4* (1), 1. https://doi.org/10.5411/wji.v4.i1.1.

- (16) Vatansever, F.; Hamblin, M. R. Photodynamic Therapy and Antitumor Immune Response. In *Cancer Immunology*; Rezaei, N., Ed.; Springer Berlin Heidelberg: Berlin, Heidelberg, 2015; pp 383–399. https://doi.org/10.1007/978-3-662-44946-2 21.
- (17) Yang, Y.; Hu, Y.; Wang, H. Targeting Antitumor Immune Response for Enhancing the Efficacy of Photodynamic Therapy of Cancer: Recent Advances and Future Perspectives. *Oxid. Med. Cell. Longev.* **2016**, *2016*, 1–11. https://doi.org/10.1155/2016/5274084.
- (18) Hwang, H. S.; Shin, H.; Han, J.; Na, K. Combination of Photodynamic Therapy (PDT) and Anti-Tumor Immunity in Cancer Therapy. *J. Pharm. Investig.* **2018**, *48* (2), 143–151. https://doi.org/10.1007/s40005-017-0377-x.
- (19) Korbelik, M. Role of Cell Stress Signaling Networks in Cancer Cell Death and Antitumor Immune Response Following Proteotoxic Injury Inflicted by Photodynamic Therapy: TUMOR AND HOST RESPONSE TO PDT AND BCG. Lasers Surg. Med. 2018, 50 (5), 491–498. https://doi.org/10.1002/lsm.22810.
- (20) Kaleta-Richter, M.; Kawczyk-Krupka, A.; Aebisher, D.; Bartusik-Aebisher, D.; Czuba, Z.; Cieślar, G. The Capability and Potential of New Forms of Personalized Colon Cancer Treatment: Immunotherapy and Photodynamic Therapy. *Photodiagnosis Photodyn. Ther.* **2019**, *25*, 253–258. https://doi.org/10.1016/j.pdpdt.2019.01.004.
- (21) Nath, S.; Obaid, G.; Hasan, T. The Course of Immune Stimulation by Photodynamic Therapy: Bridging Fundamentals of Photochemically Induced Immunogenic Cell Death to the Enrichment of T-Cell Repertoire. *Photochem. Photobiol.* **2019**, *95* (6), 1288–1305. https://doi.org/10.1111/php.13173.
- (22) Falk-Mahapatra, R.; Gollnick, S. O. Photodynamic Therapy and Immunity: An Update. *Photochem. Photobiol.* **2020**, *96*, 550–559. https://doi.org/10.1111/php.13253.
- (23) Alzeibak, R.; Mishchenko, T. A.; Shilyagina, N. Y.; Balalaeva, I. V.; Vedunova, M. V.; Krysko, D. V. Targeting Immunogenic Cancer Cell Death by Photodynamic Therapy: Past, Present and Future. *J. Immunother. Cancer* **2021**, *9* (1), e001926. https://doi.org/10.1136/jitc-2020-001926.
- (24) Abdel-Hady, E. S.; Martin-Hirsch, P.; Duggan-Keen, M.; Stern, P. L.; Moore, J. V.; Corbitt, G.; Kitchener, H. C.; Hampson, I. N. Immunological and Viral Factors Associated with the Response of Vulval Intraepithelial Neoplasia to Photodynamic Therapy. *Cancer Res.* **2001**, *61* (1), 192–196.
- (25) Thong, P. S.-P.; Ong, K.-W.; Goh, N. S.-G.; Kho, K.-W.; Manivasager, V.; Bhuvaneswari, R.; Olivo, M.; Soo, K.-C. Photodynamic-Therapy-Activated Immune Response against Distant Untreated Tumours in Recurrent Angiosarcoma. *Lancet Oncol.* **2007**, *8* (10), 950–952. https://doi.org/10.1016/S1470-2045(07)70318-2.
- (26) Thong, P. S. P.; Olivo, M.; Kho, K.-W.; Bhuvaneswari, R.; Chin, W. W. L.; Ong, K.-W.; Soo, K.-C. Immune Response against Angiosarcoma Following Lower Fluence Rate Clinical Photodynamic Therapy. *J. Environ. Pathol. Toxicol. Oncol. Off. Organ Int. Soc. Environ. Toxicol. Cancer* **2008**, 27 (1), 35–42.
- (27) Kabingu, E.; Oseroff, A. R.; Wilding, G. E.; Gollnick, S. O. Enhanced Systemic Immune Reactivity to a Basal Cell Carcinoma Associated Antigen Following Photodynamic Therapy. *Clin. Cancer Res.* **2009**, *15* (13), 4460–4466. https://doi.org/10.1158/1078-0432.CCR-09-0400.
- (28) Morrison, S. A.; Hill, S. L.; Rogers, G. S.; Graham, R. A. Efficacy and Safety of Continuous Low-Irradiance Photodynamic Therapy in the Treatment of Chest Wall Progression of Breast Cancer. *J. Surg. Res.* 2014, 192 (2), 235–241. https://doi.org/10.1016/j.jss.2014.06.030.
- (29) Santos, L. L.; Oliveira, J.; Monteiro, E.; Santos, J.; Sarmento, C. Treatment of Head and Neck Cancer with Photodynamic Therapy with Redaporfin: A Clinical Case Report. *Case Rep. Oncol.* **2018**, *11* (3), 769–776. https://doi.org/10.1159/000493423.

- (30) Rankin, E. B.; Giaccia, A. J. Hypoxic Control of Metastasis. *Science* **2016**, *352* (6282), 175–180. https://doi.org/10.1126/science.aaf4405.
- (31) Deep, G.; Schlaepfer, I. R. Aberrant Lipid Metabolism Promotes Prostate Cancer: Role in Cell Survival under Hypoxia and Extracellular Vesicles Biogenesis. *Int. J. Mol. Sci.* **2016**, 17 (7). https://doi.org/10.3390/ijms17071061.
- (32) Mistry, I. N.; Thomas, M.; Calder, E. D. D.; Conway, S. J.; Hammond, E. M. Clinical Advances of Hypoxia-Activated Prodrugs in Combination With Radiation Therapy. *Int. J. Radiat. Oncol.* **2017**, *98* (5), 1183–1196. https://doi.org/10.1016/j.ijrobp.2017.03.024.
- (33) Fiedler, E. C.; Hemann, M. T. Aiding and Abetting: How the Tumor Microenvironment Protects Cancer from Chemotherapy. *Annu. Rev. Cancer Biol.* **2019**, *3* (1), 409–428. https://doi.org/10.1146/annurev-cancerbio-030518-055524.
- (34) Macharia, L. W.; Wanjiru, C. M.; Mureithi, M. W.; Pereira, C. M.; Ferrer, V. P.; Moura-Neto, V. MicroRNAs, Hypoxia and the Stem-Like State as Contributors to Cancer Aggressiveness. *Front. Genet.* **2019**, *10*, 125. https://doi.org/10.3389/fgene.2019.00125.
- (35) Juris, A.; Balzani, V.; Barigelletti, F.; Campagna, S.; Belser, P.; von Zelewsky, A. Ru(II) Polypyridine Complexes: Photophysics, Photochemistry, Eletrochemistry, and Chemiluminescence. *Coord. Chem. Rev.* 1988, 84, 85–277. https://doi.org/10.1016/0010-8545(88)80032-8.
- (36) Kalyanasundaram, K. *Photochemistry of Polypyridine and Porphyrin Complexes*; Acad. Pr: London, 1992.
- (37) Balzani, V.; Juris, A.; Venturi, M.; Campagna, S.; Serroni, S. Luminescent and Redox-Active Polynuclear Transition Metal Complexes. *Chem Rev* **1996**, *96* (2), 759–834. https://doi.org/10.1021/cr941154y.
- (38) Balzani, V.; Credi, A.; Venturi, M. Photochemistry and Photophysics of Coordination Compounds: An Extended View. *Coord. Chem. Rev.* **1998**, *171*, 3–16. https://doi.org/10.1016/S0010-8545(98)90005-4.
- (39) Balzani, V.; Juris, A. Photochemistry and Photophysics of Ru(II) Polypyridine Complexes in the Bologna Group. From Early Studies to Recent Developments. *Coord. Chem. Rev.* **2001**, *211* (1), 97–115. https://doi.org/10.1016/S0010-8545(00)00274-5.
- (40) McClenaghan, N. D.; Leydet, Y.; Maubert, B.; Indelli, M. T.; Campagna, S. Excited-State Equilibration: A Process Leading to Long-Lived Metal-to-Ligand Charge Transfer Luminescence in Supramolecular Systems. *Coord. Chem. Rev.* **2005**, *249* (13–14), 1336–1350. https://doi.org/10.1016/j.ccr.2004.12.017.
- (41) Campagna, S.; Puntoriero, F.; Nastasi, F.; Bergamini, G.; Balzani, V. Photochemistry and Photophysics of Coordination Compounds: Ruthenium. In *Photochemistry and Photophysics of Coordination Compounds I*; Balzani, V., Campagna, S., Eds.; Topics in Current Chemistry; Springer Berlin Heidelberg: Heidelberg, 2007; pp 117–214.
- (42) Sun, Y.; Heidary, D. K.; Zhang, Z.; Richards, C. I.; Glazer, E. C. Bacterial Cytological Profiling Reveals the Mechanism of Action of Anticancer Metal Complexes. *Mol. Pharm.* 2018, 15 (8), 3404–3416. https://doi.org/10.1021/acs.molpharmaceut.8b00407.
- (43) Cuello-Garibo, J.-A.; Meijer, M. S.; Bonnet, S. To Cage or to Be Caged? The Cytotoxic Species in Ruthenium-Based Photoactivated Chemotherapy Is Not Always the Metal. *Chem. Commun.* **2017**, *53* (50), 6768–6771. https://doi.org/10.1039/C7CC03469E.
- (44) Azar, D. F.; Audi, H.; Farhat, S.; El-Sibai, M.; Abi-Habib, R. J.; Khnayzer, R. S. Phototoxicity of Strained Ru(II) Complexes: Is It the Metal Complex or the Dissociating Ligand? *Dalton Trans.* **2017**, *46* (35), 11529–11532. https://doi.org/10.1039/C7DT02255G.
- (45) Howerton, B. S.; Heidary, D. K.; Glazer, E. C. Strained Ruthenium Complexes Are Potent Light-Activated Anticancer Agents. *J. Am. Chem. Soc.* **2012**, *134* (20), 8324–8327. https://doi.org/10.1021/ja3009677.

- (46) Heidary, D. K.; Glazer, E. C. A Light-Activated Metal Complex Targets Both DNA and RNA in a Fluorescent in Vitro Transcription and Translation Assay. *ChemBioChem* **2014**, 15 (4), 507–511. https://doi.org/10.1002/cbic.201300681.
- (47) Dickerson, M.; Howerton, B.; Bae, Y.; C. Glazer, E. Light-Sensitive Ruthenium Complex-Loaded Cross-Linked Polymeric Nanoassemblies for the Treatment of Cancer. *J. Mater. Chem. B* **2016**, *4* (3), 394–408. https://doi.org/10.1039/C5TB01613D.
- (48) Kohler, L.; Nease, L.; Vo, P.; Garofolo, J.; Heidary, D. K.; Thummel, R. P.; Glazer, E. C. Photochemical and Photobiological Activity of Ru(II) Homoleptic and Heteroleptic Complexes Containing Methylated Bipyridyl-Type Ligands. *Inorg. Chem.* **2017**, *56* (20), 12214–12223. https://doi.org/10.1021/acs.inorgchem.7b01642.
- (49) Havrylyuk, D.; Deshpande, M.; Parkin, S.; Glazer, E. C. Ru(II) Complexes with Diazine Ligands: Electronic Modulation of the Coordinating Group Is Key to the Design of "Dual Action" Photoactivated Agents. *Chem. Commun.* **2018**, *54* (88), 12487–12490. https://doi.org/10.1039/C8CC05809A.
- (50) Hidayatullah, A. N.; Wachter, E.; Heidary, D. K.; Parkin, S.; Glazer, E. C. Photoactive Ru(II) Complexes With Dioxinophenanthroline Ligands Are Potent Cytotoxic Agents. *Inorg. Chem.* **2014**, *53* (19), 10030–10032. https://doi.org/10.1021/ic5017164.
- (51) Havrylyuk, D.; Heidary, D. K.; Nease, L.; Parkin, S.; Glazer, E. C. Photochemical Properties and Structure-Activity Relationships of Ru ^{II} Complexes with Pyridylbenzazole Ligands as Promising Anticancer Agents. *Eur. J. Inorg. Chem.* **2017**, *2017* (12), 1687–1694. https://doi.org/10.1002/ejic.201601450.
- (52) Havrylyuk, D.; Stevens, K.; Parkin, S.; Glazer, E. C. Toward Optimal Ru(II) Photocages: Balancing Photochemistry, Stability, and Biocompatibility Through Fine Tuning of Steric, Electronic, and Physiochemical Features. *Inorg. Chem.* **2020**, *59* (2), 1006–1013. https://doi.org/10.1021/acs.inorgchem.9b02065.
- (53) Albani, B. A.; Durr, C. B.; Turro, C. Selective Photoinduced Ligand Exchange in a New Tris-Heteroleptic Ru(II) Complex. *J. Phys. Chem. A* **2013**, *117* (50), 13885–13892. https://doi.org/10.1021/jp4085684.
- (54) Loftus, L. M.; White, J. K.; Albani, B. A.; Kohler, L.; Kodanko, J. J.; Thummel, R. P.; Dunbar, K. R.; Turro, C. New Ru^{II} Complex for Dual Activity: Photoinduced Ligand Release and ¹O₂ Production. *Chem. Eur. J.* **2016**, *22* (11), 3704–3708. https://doi.org/10.1002/chem.201504800.
- (55) Knoll, J. D.; Albani, B. A.; Durr, C. B.; Turro, C. Unusually Efficient Pyridine Photodissociation from Ru(II) Complexes with Sterically Bulky Bidentate Ancillary Ligands. *J. Phys. Chem. A* **2014**, *118* (45), 10603–10610. https://doi.org/10.1021/jp5057732.
- (56) Arora, K.; White, J. K.; Sharma, R.; Mazumder, S.; Martin, P. D.; Schlegel, H. B.; Turro, C.; Kodanko, J. J. Effects of Methyl Substitution in Ruthenium Tris(2-Pyridylmethyl)Amine Photocaging Groups for Nitriles. *Inorg. Chem.* **2016**, *55* (14), 6968–6979. https://doi.org/10.1021/acs.inorgchem.6b00650.
- (57) Huisman, M.; White, J. K.; Lewalski, V. G.; Podgorski, I.; Turro, C.; Kodanko, J. J. Caging the Uncageable: Using Metal Complex Release for Photochemical Control over Irreversible Inhibition. *Chem. Commun.* 2016, 52 (85), 12590–12593. https://doi.org/10.1039/C6CC07083C.
- (58) Li, A.; Yadav, R.; White, J. K.; Herroon, M. K.; Callahan, B. P.; Podgorski, I.; Turro, C.; Scott, E. E.; Kodanko, J. J. Illuminating Cytochrome P450 Binding: Ru(II)-Caged Inhibitors of CYP17A1. *Chem. Commun.* **2017**, *53* (26), 3673–3676. https://doi.org/10.1039/C7CC01459G.
- (59) Arora, K.; Herroon, M.; Al-Afyouni, M. H.; Toupin, N. P.; Rohrabaugh, T. N.; Loftus, L. M.; Podgorski, I.; Turro, C.; Kodanko, J. J. Catch and Release Photosensitizers: Combining Dual-Action Ruthenium Complexes with Protease Inactivation for Targeting Invasive

- Cancers. J. Am. Chem. Soc. **2018**, 140 (43), 14367–14380. https://doi.org/10.1021/jacs.8b08853.
- (60) Li, A.; Turro, C.; Kodanko, J. J. Ru(II) Polypyridyl Complexes as Photocages for Bioactive Compounds Containing Nitriles and Aromatic Heterocycles. *Chem. Commun.* **2018**, *54* (11), 1280–1290. https://doi.org/10.1039/C7CC09000E.
- (61) Li, A.; Turro, C.; Kodanko, J. J. Ru(II) Polypyridyl Complexes Derived from Tetradentate Ancillary Ligands for Effective Photocaging. *Acc. Chem. Res.* **2018**, *51* (6), 1415–1421. https://doi.org/10.1021/acs.accounts.8b00066.
- (62) Nisbett, K.; Tu, Y.-J.; Turro, C.; Kodanko, J. J.; Schlegel, H. B. DFT Investigation of Ligand Photodissociation in [Rull(Tpy)(Bpy)(Py)]2+ and [Rull(Tpy)(Me2bpy)(Py)]2+ Complexes. *Inorg. Chem.* **2018**, *57* (1), 231–240. https://doi.org/10.1021/acs.inorgchem.7b02398.
- (63) Rohrabaugh, T. N.; Rohrabaugh, A. M.; Kodanko, J. J.; White, J. K.; Turro, C. Photoactivation of Imatinib–Antibody Conjugate Using Low-Energy Visible Light from Ru(II)-Polypyridyl Cages. *Chem. Commun.* **2018**, *54* (41), 5193–5196. https://doi.org/10.1039/C8CC01348A.
- (64) Toupin, N. P.; Nadella, S.; Steinke, S. J.; Turro, C.; Kodanko, J. J. Dual-Action Ru(II) Complexes with Bulky π-Expansive Ligands: Phototoxicity without DNA Intercalation. *Inorg. Chem.* 2020, 59 (6), 3919–3933. https://doi.org/10.1021/acs.inorgchem.9b03585.
- (65) Bahreman, A.; Limburg, B.; Siegler, M. A.; Bouwman, E.; Bonnet, S. Spontaneous Formation in the Dark, and Visible Light-Induced Cleavage, of a Ru–S Bond in Water: A Thermodynamic and Kinetic Study. *Inorg. Chem.* 2013, 52 (16), 9456–9469. https://doi.org/10.1021/ic401105v.
- (66) Bahreman, A.; Rabe, M.; Kros, A.; Bruylants, G.; Bonnet, S. Binding of a Ruthenium Complex to a Thioether Ligand Embedded in a Negatively Charged Lipid Bilayer: A Two-Step Mechanism. *Chem. - Eur. J.* 2014, 20 (24), 7429–7438. https://doi.org/10.1002/chem.201400377.
- (67) Göttle, A. J.; Alary, F.; Boggio-Pasqua, M.; Dixon, I. M.; Heully, J.-L.; Bahreman, A.; Askes, S. H. C.; Bonnet, S. Pivotal Role of a Pentacoordinate ³MC State on the Photocleavage Efficiency of a Thioether Ligand in Ruthenium(II) Complexes: A Theoretical Mechanistic Study. *Inorg. Chem.* **2016**, *55* (9), 4448–4456. https://doi.org/10.1021/acs.inorgchem.6b00268.
- (68) Lameijer, L. N.; Ernst, D.; Hopkins, S. L.; Meijer, M. S.; Askes, S. H. C.; Le Dévédec, S. E.; Bonnet, S. A Red-Light-Activated Ruthenium-Caged NAMPT Inhibitor Remains Phototoxic in Hypoxic Cancer Cells. *Angew. Chem. Int. Ed.* **2017**, *56* (38), 11549–11553. https://doi.org/10.1002/anie.201703890.
- (69) Cuello-Garibo, J.-A.; Pérez-Gallent, E.; van der Boon, L.; Siegler, M. A.; Bonnet, S. Influence of the Steric Bulk and Solvent on the Photoreactivity of Ruthenium Polypyridyl Complexes Coordinated to L-Proline. *Inorg. Chem.* **2017**, *56* (9), 4818–4828. https://doi.org/10.1021/acs.inorgchem.6b02794.
- (70) Sun, W.; Wen, Y.; Thiramanas, R.; Chen, M.; Han, J.; Gong, N.; Wagner, M.; Jiang, S.; Meijer, M. S.; Bonnet, S.; Butt, H.-J.; Mailänder, V.; Liang, X.-J.; Wu, S. Red-Light-Controlled Release of Drug-Ru Complex Conjugates from Metallopolymer Micelles for Phototherapy in Hypoxic Tumor Environments. *Adv. Funct. Mater.* 2018, 28 (39), 1804227. https://doi.org/10.1002/adfm.201804227.
- (71) Meijer, M. S.; Talens, V. S.; Hilbers, M. F.; Kieltyka, R. E.; Brouwer, A. M.; Natile, M. M.; Bonnet, S. NIR-Light-Driven Generation of Reactive Oxygen Species Using Ru(II)-Decorated Lipid-Encapsulated Upconverting Nanoparticles. *Langmuir* 2019, 35 (37), 12079–12090. https://doi.org/10.1021/acs.langmuir.9b01318.

- (72) Al-Afyouni, M. H.; Rohrabaugh, T. N.; Al-Afyouni, K. F.; Turro, C. New Ru(II) Photocages Operative with near-IR Light: New Platform for Drug Delivery in the PDT Window. *Chem. Sci.* **2018**, 9 (32), 6711–6720. https://doi.org/10.1039/C8SC02094A.
- (73) Feng, W.; Gao, C.; Liu, W.; Ren, H.; Wang, C.; Ge, K.; Li, S.; Zhou, G.; Li, H.; Wang, S.; Jia, G.; Li, Z.; Zhang, J. A Novel Anticancer Theranostic Pro-Prodrug Based on Hypoxia and Photo Sequential Control. *Chem Commun* **2016**, *52* (60), 9434–9437. https://doi.org/10.1039/C6CC02932A.
- (74) Li, M.-D.; Wong, N.-K.; Xiao, J.; Zhu, R.; Wu, L.; Dai, S.-Y.; Chen, F.; Huang, G.; Xu, L.; Bai, X.; Geraskina, M. R.; Winter, A. H.; Chen, X.; Liu, Y.; Fang, W.; Yang, D.; Phillips, D. L. Dynamics of Oxygen-Independent Photocleavage of Blebbistatin as a One-Photon Blue or Two-Photon Near-Infrared Light-Gated Hydroxyl Radical Photocage. *J. Am. Chem. Soc.* **2018**, *140* (46), 15957–15968. https://doi.org/10.1021/jacs.8b10235.
- (75) van Rixel, V. H. S.; Ramu, V.; Auyeung, A. B.; Beztsinna, N.; Leger, D. Y.; Lameijer, L. N.; Hilt, S. T.; Le Dévédec, S. E.; Yildiz, T.; Betancourt, T.; Gildner, M. B.; Hudnall, T. W.; Sol, V.; Liagre, B.; Kornienko, A.; Bonnet, S. Photo-Uncaging of a Microtubule-Targeted Rigidin Analogue in Hypoxic Cancer Cells and in a Xenograft Mouse Model. *J. Am. Chem. Soc.* 2019, 141 (46), 18444–18454. https://doi.org/10.1021/jacs.9b07225.
- (76) Roque, J.; Havrylyuk, D.; Barrett, P. C.; Sainuddin, T.; McCain, J.; Colón, K.; Sparks, W. T.; Bradner, E.; Monro, S.; Heidary, D.; Cameron, C. G.; Glazer, E. C.; McFarland, S. A. Strained, Photoejecting Ru(II) Complexes That Are Cytotoxic Under Hypoxic Conditions. *Photochem. Photobiol.* **2020**, *96* (2), 327–339. https://doi.org/10.1111/php.13174.
- (77) Cole, H. D.; Roque, J. A.; Lifshits, L. M.; Hodges, R.; Barrett, P. C.; Havrylyuk, D.; Heidary, D.; Ramasamy, E.; Cameron, C. G.; Glazer, E. C.; McFarland, S. A. Fine-Feature Modifications to Strained Ruthenium Complexes Radically Alter Their Hypoxic Anticancer Activity †. *Photochem. Photobiol.* **2022**, *98* (1), 73–84. https://doi.org/10.1111/php.13395.
- (78) Cole, H. D.; Roque, J. A.; Shi, G.; Lifshits, L. M.; Ramasamy, E.; Barrett, P. C.; Hodges, R. O.; Cameron, C. G.; McFarland, S. A. Anticancer Agent with Inexplicable Potency in Extreme Hypoxia: Characterizing a Light-Triggered Ruthenium Ubertoxin. *J. Am. Chem. Soc.* **2021**, jacs.1c09010. https://doi.org/10.1021/jacs.1c09010.
- (79) Roque III, J. A.; Barrett, P. C.; Cole, H. D.; Lifshits, L. M.; Shi, G.; Monro, S.; von Dohlen, D.; Kim, S.; Russo, N.; Deep, G.; Cameron, C. G.; Alberto, M. E.; McFarland, S. A. Breaking the Barrier: An Osmium Photosensitizer with Unprecedented Hypoxic Phototoxicity for Real World Photodynamic Therapy. *Chem. Sci.* **2020**, *11*, 9784–9806. https://doi.org/10.1039/D0SC03008B.
- (80) Roque, J. A.; Barrett, P. C.; Cole, H. D.; Lifshits, L. M.; Bradner, E.; Shi, G.; von Dohlen, D.; Kim, S.; Russo, N.; Deep, G.; Cameron, C. G.; Alberto, M. E.; McFarland, S. A. Os(II) Oligothienyl Complexes as a Hypoxia-Active Photosensitizer Class for Photodynamic Therapy. *Inorg. Chem.* **2020**, *59* (22), 16341–16360. https://doi.org/10.1021/acs.inorgchem.0c02137.
- (81) Lv, Z.; Wei, H.; Li, Q.; Su, X.; Liu, S.; Zhang, K. Y.; Lv, W.; Zhao, Q.; Li, X.; Huang, W. Achieving Efficient Photodynamic Therapy under Both Normoxia and Hypoxia Using Cyclometalated Ru(II) Photosensitizer through Type I Photochemical Process. *Chem. Sci.* **2018**, 9 (2), 502–512. https://doi.org/10.1039/C7SC03765A.
- (82) Yu, Q.; Huang, T.; Liu, C.; Zhao, M.; Xie, M.; Li, G.; Liu, S.; Huang, W.; Zhao, Q. Oxygen Self-Sufficient NIR-Activatable Liposomes for Tumor Hypoxia Regulation and Photodynamic Therapy. *Chem. Sci.* **2019**, *10* (39), 9091–9098. https://doi.org/10.1039/C9SC03161H.
- (83) Evans, C. L.; Abu-Yousif, A. O.; Park, Y. J.; Klein, O. J.; Celli, J. P.; Rizvi, I.; Zheng, X.; Hasan, T. Killing Hypoxic Cell Populations in a 3D Tumor Model with EtNBS-PDT. PLoS ONE 2011, 6 (8), e23434. https://doi.org/10.1371/journal.pone.0023434.

- (84) Kuang, S.; Wei, F.; Karges, J.; Ke, L.; Xiong, K.; Liao, X.; Gasser, G.; Ji, L.; Chao, H. Photodecaging of a Mitochondria-Localized Iridium(III) Endoperoxide Complex for Two-Photon Photoactivated Therapy under Hypoxia. *J. Am. Chem. Soc.* 2022, 4091–4101. https://doi.org/10.1021/jacs.1c13137.
- (85) Mazuryk, O.; Janczy-Cempa, E.; Łagosz, J.; Rutkowska-Zbik, D.; Machnicka, A.; Krasowska, A.; Pietrzyk, P.; Stochel, G.; Brindell, M. Relevance of the Electron Transfer Pathway in Photodynamic Activity of Ru(II) Polypyridyl Complexes Containing 4,7-Diphenyl-1,10-Phenanthroline Ligands under Normoxic and Hypoxic Conditions. *Dalton Trans.* 2022, *51* (5), 1888–1900. https://doi.org/10.1039/D1DT02908H.
- (86) Xiao, Y.-F.; Chen, W.-C.; Chen, J.-X.; Lu, G.; Tian, S.; Cui, X.; Zhang, Z.; Chen, H.; Wan, Y.; Li, S.; Lee, C.-S. Amplifying Free Radical Generation of AIE Photosensitizer with Small Singlet–Triplet Splitting for Hypoxia-Overcoming Photodynamic Therapy. ACS Appl. Mater. Interfaces 2022, 14 (4), 5112–5121. https://doi.org/10.1021/acsami.1c23797.
- (87) Wenger, R.; Kurtcuoglu, V.; Scholz, C.; Marti, H.; Hoogewijs, D. Frequently Asked Questions in Hypoxia Research. *Hypoxia* **2015**, *3*, 35–43. https://doi.org/10.2147/HP.S92198.
- (88) Sainuddin, T.; Pinto, M.; Yin, H.; Hetu, M.; Colpitts, J.; McFarland, S. A. Strained Ruthenium Metal–Organic Dyads as Photocisplatin Agents with Dual Action. *J. Inorg. Biochem.* **2016**, *158*, 45–54. https://doi.org/10.1016/j.jinorgbio.2016.01.009.
- (89) Wang, Z. Radziszewski Reaction. In *Comprehensive Organic Name Reactions and Reagents*; John Wiley & Sons, Inc., 2010. https://doi.org/10.1002/9780470638859.conrr518.
- (90) Ghosh, G.; Colón, K. L.; Fuller, A.; Sainuddin, T.; Bradner, E.; McCain, J.; Monro, S. M. A.; Yin, H.; Hetu, M. W.; Cameron, C. G.; McFarland, S. A. Cyclometalated Ruthenium(II) Complexes Derived from α-Oligothiophenes as Highly Selective Cytotoxic or Photocytotoxic Agents. *Inorg. Chem.* 2018, *57* (13), 7694–7712. https://doi.org/10.1021/acs.inorgchem.8b00689.
- (91) Alberto, M. E.; Pirillo, J.; Russo, N.; Adamo, C. Theoretical Exploration of Type I/Type II Dual Photoreactivity of Promising Ru(II) Dyads for PDT Approach. *Inorg. Chem.* **2016**, *55* (21), 11185–11192. https://doi.org/10.1021/acs.inorgchem.6b01782.
- (92) Lanzani, G.; Nisoli, M.; De Silvestri, S.; Tubino, R. Femtosecond Vibrational and Torsional Energy Redistribution in Photoexcited Oligothiophenes. *Chem. Phys. Lett.* **1996**, *251* (5–6), 339–345. https://doi.org/10.1016/0009-2614(96)00107-8.
- (93) Yang, J.-P.; Paa, W.; Rentsch, S. Femtosecond Investigations of Photophysics of Ultrafast Intersystem Crossing in Terthiophene by Wavelength Dependent Excitation. *Chem. Phys. Lett.* **2000**, *320* (5–6), 665–672. https://doi.org/10.1016/S0009-2614(00)00264-5.
- (94) Alberto, M. E.; De Simone, B. C.; Mazzone, G.; Sicilia, E.; Russo, N. The Heavy Atom Effect on Zn(II) Phthalocyanine Derivatives: A Theoretical Exploration of the Photophysical Properties. *Phys. Chem. Chem. Phys.* **2015**, *17* (36), 23595–23601. https://doi.org/10.1039/C5CP03833B.
- (95) Ogilby, P. R. Singlet Oxygen: There Is Still Something New under the Sun, and It Is Better than Ever. *Photochem. Photobiol. Sci.* **2010**, 9 (12), 1543. https://doi.org/10.1039/c0pp00213e.
- (96) Shi, G.; Monro, S.; Hennigar, R.; Colpitts, J.; Fong, J.; Kasimova, K.; Yin, H.; DeCoste, R.; Spencer, C.; Chamberlain, L.; Mandel, A.; Lilge, L.; McFarland, S. A. Ru(II) Dyads Derived from α-Oligothiophenes: A New Class of Potent and Versatile Photosensitizers for PDT. *Coord. Chem. Rev.* 2015, 282–283, 127–138. https://doi.org/10.1016/j.ccr.2014.04.012.
- (97) Sainuddin, T.; McCain, J.; Pinto, M.; Yin, H.; Gibson, J.; Hetu, M.; McFarland, S. A. Organometallic Ru(II) Photosensitizers Derived from π-Expansive Cyclometalating

- Ligands: Surprising Theranostic PDT Effects. *Inorg. Chem.* **2016**, *55* (1), 83–95. https://doi.org/10.1021/acs.inorgchem.5b01838.
- (98) Monro, S.; Cameron, C. G.; Zhu, X.; Colón, K. L.; Yin, H.; Sainuddin, T.; Hetu, M.; Pinto, M.; Fuller, A.; Bennett, L.; Roque, J.; Sun, W.; McFarland, S. A. Synthesis, Characterization and Photobiological Studies of Ru(II) Dyads Derived from α-Oligothiophene Derivatives of 1,10-Phenanthroline. *Photochem. Photobiol.* 2019, 95 (1), 267–279. https://doi.org/10.1111/php.13012.
- (99) Lifshits, L. M.; Roque, J. A.; Cole, H. D.; Thummel, R. P.; Cameron, C. G.; McFarland, S. A. NIR-Absorbing Ru II Complexes Containing A-Oligothiophenes for Applications in Photodynamic Therapy. *ChemBioChem* 2020, 21, 3594–3607. https://doi.org/10.1002/cbic.202000419.
- (100) Suzuki, K.; Kobayashi, A.; Kaneko, S.; Takehira, K.; Yoshihara, T.; Ishida, H.; Shiina, Y.; Oishi, S.; Tobita, S. Reevaluation of Absolute Luminescence Quantum Yields of Standard Solutions Using a Spectrometer with an Integrating Sphere and a Back-Thinned CCD Detector. *Phys. Chem. Chem. Phys.* 2009, 11 (42), 9850–9860. https://doi.org/10.1039/B912178A.
- (101) DeRosa, M. C.; Crutchley, R. J. Photosensitized Singlet Oxygen and Its Applications. *Coord. Chem. Rev.* **2002**, *233*–*234*, 351–371. https://doi.org/10.1016/S0010-8545(02)00034-6.
- (102) Bhasikuttan, A. C.; Suzuki, M.; Nakashima, S.; Okada, T. Ultrafast Fluorescence Detection in Tris(2,2'-Bipyridine)Ruthenium(II) Complex in Solution: Relaxation Dynamics Involving Higher Excited States. *J. Am. Chem. Soc.* **2002**, *124* (28), 8398–8405. https://doi.org/10.1021/ja026135h.
- (103) McCusker, J. K. Femtosecond Absorption Spectroscopy of Transition Metal Charge-Transfer Complexes. Acc. Chem. Res. 2003, 36 (12), 876–887. https://doi.org/10.1021/ar030111d.
- (104) Cannizzo, A.; van Mourik, F.; Gawelda, W.; Zgrablic, G.; Bressler, C.; Chergui, M. Broadband Femtosecond Fluorescence Spectroscopy of [Ru(Bpy)3]2+. *Angew. Chem. Int. Ed.* **2006**, *45* (19), 3174–3176. https://doi.org/10.1002/anie.200600125.
- (105) Atkins, A. J.; González, L. Trajectory Surface-Hopping Dynamics Including Intersystem Crossing in [Ru(Bpy) 3] ²⁺. *J. Phys. Chem. Lett.* **2017**, *8* (16), 3840–3845. https://doi.org/10.1021/acs.ipclett.7b01479.
- (106) Sun, Q.; Mosquera-Vazquez, S.; Lawson Daku, L. M.; Guénée, L.; Goodwin, H. A.; Vauthey, E.; Hauser, A. Experimental Evidence of Ultrafast Quenching of the 3MLCT Luminescence in Ruthenium(II) Tris-Bipyridyl Complexes via a 3dd State. *J. Am. Chem. Soc.* **2013**, *135* (37), 13660–13663. https://doi.org/10.1021/ja407225t.
- (107) Reichardt, C.; Monro, S.; Sobotta, F. H.; Colón, K. L.; Sainuddin, T.; Stephenson, M.; Sampson, E.; Roque III, J.; Yin, H.; Brendel, J. C.; Cameron, C. G.; McFarland, S.; Dietzek, B. Predictive Strength of Photophysical Measurements for in Vitro Photobiological Activity in a Series of Ru(II) Polypyridyl Complexes Derived from π-Extended Ligands. *Inorg. Chem.* 2019, *58* (5), 3156–3166. https://doi.org/10.1021/acs.inorgchem.8b03223.
- (108) Lincoln, R.; Kohler, L.; Monro, S.; Yin, H.; Stephenson, M.; Zong, R.; Chouai, A.; Dorsey, C.; Hennigar, R.; Thummel, R. P.; McFarland, S. A. Exploitation of Long-Lived 3IL Excited States for Metal–Organic Photodynamic Therapy: Verification in a Metastatic Melanoma Model. *J Am Chem Soc* **2013**, *135* (45), 17161–17175. https://doi.org/10.1021/ja408426z.
- (109) Stephenson, M.; Reichardt, C.; Pinto, M.; Wächtler, M.; Sainuddin, T.; Shi, G.; Yin, H.; Monro, S.; Sampson, E.; Dietzek, B.; McFarland, S. A. Ru(II) Dyads Derived from 2-(1-Pyrenyl)-1H-Imidazo[4,5][1,10]Phenanthroline: Versatile Photosensitizers for Photodynamic Applications. *J. Phys. Chem. A* **2014**, *118* (45), 10507–10521. https://doi.org/10.1021/jp504330s.

- (110) Yin, H.; Stephenson, M.; Gibson, J.; Sampson, E.; Shi, G.; Sainuddin, T.; Monro, S.; McFarland, S. A. In Vitro Multiwavelength PDT with 3IL States: Teaching Old Molecules New Tricks. *Inorg. Chem.* **2014**, *53* (9), 4548–4559. https://doi.org/10.1021/ic5002368.
- (111) McCain, J.; Colón, K. L.; Barrett, P. C.; Monro, S. M. A.; Sainuddin, T.; Roque III, J.; Pinto, M.; Yin, H.; Cameron, C. G.; McFarland, S. A. Photophysical Properties and Photobiological Activities of Ruthenium(II) Complexes Bearing π-Expansive Cyclometalating Ligands with Thienyl Groups. *Inorg. Chem.* **2019**, *58* (16), 10778–10790. https://doi.org/10.1021/acs.inorgchem.9b01044.
- (112) Reichardt, C.; Schneider, K. R. A.; Sainuddin, T.; Wächtler, M.; McFarland, S. A.; Dietzek, B. Excited State Dynamics of a Photobiologically Active Ru(II) Dyad Are Altered in Biologically Relevant Environments. *J. Phys. Chem. A* **2017**, *121* (30), 5635–5644. https://doi.org/10.1021/acs.jpca.7b04670.
- (113) Loftus, L. M.; Al-Afyouni, K. F.; Turro, C. New Ru^{II} Scaffold for Photoinduced Ligand Release with Red Light in the Photodynamic Therapy (PDT) Window. *Chem. Eur. J.* **2018**, *24* (45), 11550–11553. https://doi.org/10.1002/chem.201802405.
- (114) Meijer, M. S.; Bonnet, S. Diastereoselective Synthesis and Two-Step Photocleavage of Ruthenium Polypyridyl Complexes Bearing a Bis(Thioether) Ligand. *Inorg. Chem.* **2019**, *58* (17), 11689–11698. https://doi.org/10.1021/acs.inorgchem.9b01669.
- (115) Francés-Monerris, A.; Gros, P. C.; Assfeld, X.; Monari, A.; Pastore, M. Toward Luminescent Iron Complexes: Unravelling the Photophysics by Computing Potential Energy Surfaces. *ChemPhotoChem* **2019**, *3* (9), 666–683. https://doi.org/10.1002/cptc.201900100.
- (116) Soupart, A.; Alary, F.; Heully, J.-L.; Elliott, P. I. P.; Dixon, I. M. Recent Progress in Ligand Photorelease Reaction Mechanisms: Theoretical Insights Focusing on Ru(II) 3MC States. *Coord. Chem. Rev.* **2020**, *408*, 213184. https://doi.org/10.1016/j.ccr.2020.213184.
- (117) Francés-Monerris, A.; Magra, K.; Darari, M.; Cebrián, C.; Beley, M.; Domenichini, E.; Haacke, S.; Pastore, M.; Assfeld, X.; Gros, P. C.; Monari, A. Synthesis and Computational Study of a Pyridylcarbene Fe(II) Complex: Unexpected Effects of *Fac/ Mer Isomerism* in Metal-to-Ligand Triplet Potential Energy Surfaces. *Inorg. Chem.* **2018**, *57* (16), 10431–10441. https://doi.org/10.1021/acs.inorgchem.8b01695.
- (118) Magra, K.; Domenichini, E.; Francés-Monerris, A.; Cebrián, C.; Beley, M.; Darari, M.; Pastore, M.; Monari, A.; Assfeld, X.; Haacke, S.; Gros, P. C. Impact of the *Fac/Mer* Isomerism on the Excited-State Dynamics of Pyridyl-Carbene Fe(II) Complexes. *Inorg. Chem.* **2019**, *58* (8), 5069–5081. https://doi.org/10.1021/acs.inorgchem.9b00138.
- (119) Magra, K.; Darari, M.; Domenichini, E.; Francés-Monerris, A.; Cebrián, C.; Beley, M.; Pastore, M.; Monari, A.; Assfeld, X.; Haacke, S.; Gros, P. C. Photophysical Investigation of Iron(II) Complexes Bearing Bidentate Annulated Isomeric Pyridine-NHC Ligands. *J. Phys. Chem. C* 2020, 124 (34), 18379–18389. https://doi.org/10.1021/acs.jpcc.0c03638.
- (120) Neese, F. Software Update: The ORCA Program System, Version 4.0. *WIREs Comput. Mol. Sci.* **2018**, *8* (1). https://doi.org/10.1002/wcms.1327.
- (121) Zhu, X.; Thompson, K. C.; Martínez, T. J. Geodesic Interpolation for Reaction Pathways. *J. Chem. Phys.* **2019**, *150* (16), 164103. https://doi.org/10.1063/1.5090303.
- (122) Ford, W. E.; Rodgers, M. A. J. Reversible Triplet-Triplet Energy Transfer within a Covalently Linked Bichromophoric Molecule. *J. Phys. Chem.* **1992**, *96* (7), 2917–2920. https://doi.org/10.1021/j100186a026.
- (123) Wilson, G. J.; Launikonis, A.; Sasse, W. H. F.; Mau, A. W.-H. Excited-State Processes in Ruthenium(II) Bipyridine Complexes Containing Covalently Bound Arenes. *J. Phys. Chem. A* **1997**, *101* (27), 4860–4866. https://doi.org/10.1021/jp970667g.
- (124) Tyson, D. S.; Castellano, F. N. Intramolecular Singlet and Triplet Energy Transfer in a Ruthenium(II) Diimine Complex Containing Multiple Pyrenyl Chromophores. *J Phys Chem A* **1999**, *103* (50), 10955–10960. https://doi.org/10.1021/jp992983w.

- (125) Morales, A. F.; Accorsi, G.; Armaroli, N.; Barigelletti, F.; Pope, S. J. A.; Ward, M. D. Interplay of Light Antenna and Excitation "Energy Reservoir" Effects in a Bichromophoric System Based on Ruthenium–Polypyridine and Pyrene Units Linked by a Long and Flexible Poly(Ethylene Glycol) Chain. *Inorg. Chem.* **2002**, *41* (25), 6711–6719. https://doi.org/10.1021/ic025811d.
- (126) Hachey, A. C.; Havrylyuk, D.; Glazer, E. C. Biological Activities of Polypyridyl-Type Ligands: Implications for Bioinorganic Chemistry and Light-Activated Metal Complexes. *Curr. Opin. Chem. Biol.* **2021**, *61*, 191–202. https://doi.org/10.1016/j.cbpa.2021.01.016.

TOC GRAPHIC

